Taylor Jacovich
Physics 460
Dr. Milingo
11/13/14

Activity-Cycle Viability of Kepler Input Catalog Stars in NGC 6811

Abstract:

Presented are the results of a stellar activity-cycle viability study of three Kepler Input Catalog stars located within the Open Cluster NGC 6811. The three stars: KIC9655315, KIC9715987, and KIC9716650 were observed utilizing the Gettysburg College Observatory 0.4m telescope from May to October 2007, and the National Undergraduate Research Observatory 0.8m telescope in June 2013 and June 2014. All available photometric data from the Kepler Archive was also examined to attempt to supplement and contextualize these observations. Rotational periods were determined utilizing a Lomb-Scargle period-finding routine. The GCO and NURO data were not directly conclusive, but from the Kepler data, it was found that KIC9655315 was the most likely candidate of the three stars for continued observation. KIC9655315 displayed the most stable lightcurve, with few anomalies and a very definitive rotational period. KIC9716650 and KIC9715987 both exhibited photometric anomalies that complicated the lightcurves and would make them more difficult to observe with the GCO and NURO telescopes.

Introduction

Stellar activity is a magnetic phenomenon present in low-mass main sequence stars, or cool dwarfs, like our sun. On the sun, activity is responsible for many processes such as sunspots, solar flares, solar prominences, and coronal mass ejections.[1] These are all intimately connected to continued human existence, being able to negatively impact things such as these electrical grid, as well as satellite and ground based wireless communications. With such phenomena in play, the ultimate goal of understanding activity cycles would be to predict and prepare for such events.[2]

Predictions require building a parameter space based on empirical data for all cool dwarfs, and applying this to the time evolution of the sun. This would allow the characterization of the solar dynamo, the driving force behind all magnetic activity.

Activity cycle observations often take decades to complete, as the star must have progressed sufficiently within its cycle for modern photometric techniques to be able to definitively identify it. Because of this, it is important to first survey the candidate stars, and attempt to identify stars with sufficiently detectable and relatively stable rotational activity. This paper details the viability of three Kepler field stars, KIC9655315, KIC9715987, and KIC9716650.

Theoretical Overview

The activity cycle of a star is closely linked to its mass, age, and rotational period.[3] As a result, these factors would be most useful in creating the activity-cycle parameter space described above. None of these values can be directly detected for a star, but they can be inferred through observable properties of main sequence stars and star clusters.

Main sequence stars are massive, gravitationally bound, objects. Like the universe, they are composed largely of hydrogen and helium along with trace amounts of metals.[4] Energy from gravitational compression maintains these elements in a plasma state. The high-temperature and high-pressure environment of the stellar core gives rise to hydrogen fusion within the plasma. Outward pressure from core fusion retards the gravitational compression of the star, and keeps it in a state of hydrostatic equilibrium.[4]

Empirical means can be used to define the relationship of stars in hydrostatic equilibrium and observable characteristics. The most obvious of these would be the Hertzsprung-Russell diagram.[4]

Hetzsprung-Russell diagrams, or HR diagrams for short, relate the surface temperature of a star to the luminosity, or some corollary of these two parameters.[4] The

equilibrium point of the forces contributed by core fusion and gravitational collapse determine both the effective temperature of the stellar surface, which acts as a blackbody radiator, and the volume of the star. Stellar temperature can be determined directly utilizing Wein's Law[4]:

$$T_{eff} = \frac{2.9x10^6\ nm * K}{\lambda_{max}}$$

where T_{eff} is the surface temperature of the star, λ_{max} is the peak output of the stellar spectral density curve in nanometers, and $2.9x10^6\ nm * K$ is a constant.

Stellar luminosity can be derived from this result and the surface area of the star. Starting with the Stefan-Boltzmann law for flux, and combining it with the amount of surface area radiating with that flux, it becomes clear that Luminosity can be written as

$$L = 4\pi r^2 \sigma {T_{eff}}^4$$

where L is the luminosity of the star, $4\pi r^2$ is the surface area, and $\sigma {T_{eff}}^4$ is the Stefan-Boltzmann Law with $\sigma = 5.67037321{\times}10^{-8}\ \mathrm{W}m^{-2}K^{-4}$.[4] These two equations allow for the construction of the HR diagram in terms of values related to the mass of the star through hydrostatic equilibrium. An HR diagram is included in figure 1.[5] It is important to note that stars undergoing hydrogen fusion exist along the central diagonal line of this diagram. For stars along the main-sequence line, a computational relationship between mass and luminosity was derived[4]:

$$\frac{L}{L_{sun}} = \left(\frac{M}{M_{sun}}\right)^{3.5}$$

Here, L is the luminosity of the star, M is the mass of the observed star, and L_{sun} and M_{sun} are the mass and luminosity of the sun. This equation is not entirely accurate, and breaks down as stellar masses move further from the Sun's, but it is still useful for understanding the basic relationship between stellar mass and observables. Other stars, such as those that would be considered red supergiants have moved beyond purely hydrogen fusion and have begun fusing heavier elements. This alters the equilibrium forces within the star, changing the relationship between *L* and stellar mass.[6] This manifests as an increase in surface area for a given temperature, altering the stellar luminosity and shifting it higher on the HR diagram.

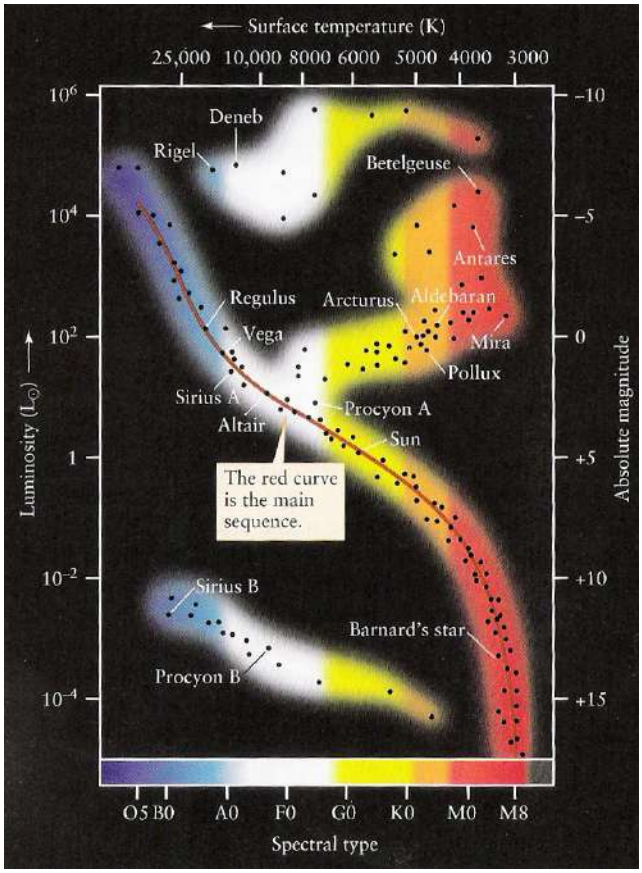

Figure 1: Hertzsprung-Russell diagram[5]

HR diagrams can also be used for determining stellar ages. Associations of stars known as Open Clusters are gravitational bound groups of stars that formed from the same nebula at roughly the same time.[4] The only difference between stars in these clusters is a variation in stellar mass. These variations allow an H-R diagram to be made from the members of open clusters, and for a main-sequence line to be fitted along the diagram. Unlike in the general H-R diagram, the diagram of the cluster will only extend along the main sequence to a specific point. At this point, the population of stars will diverge from

the main sequence, and tend toward the lower surface temperature, high luminosity portion of the diagram, as shown in figure 2.[7]

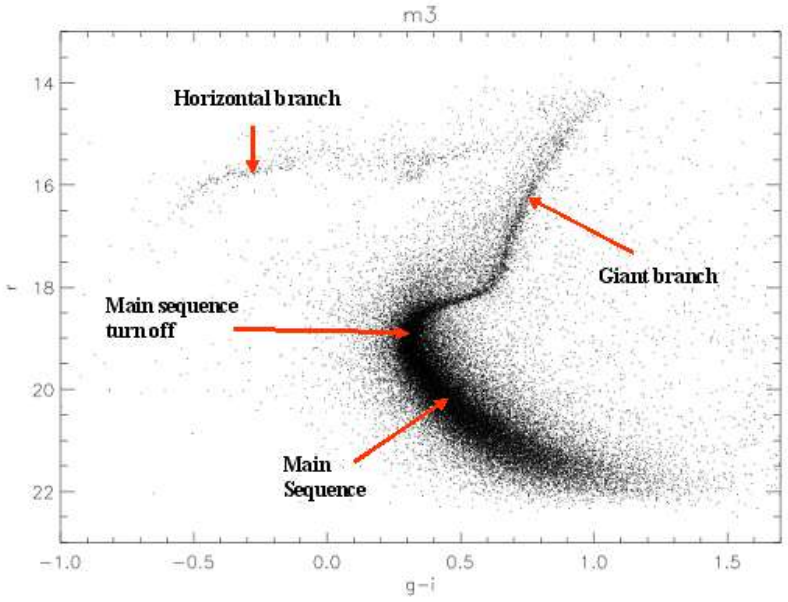

Figure 2: H-R diagram of an Open Cluster[7]

This diversion is indicative of more massive stars having shorter lifespans, a logical conclusion given that more massive stars must fuse several times more hydrogen to maintain hydrostatic equilibrium. For precision measurements, a stellar isochrone is fitted that follows the population of stars exactly.[8] Isochrones are lines that represent stars of equal ages, something present in a cluster, and the divergence point can be used to calculate the cluster age. The isochrone fitting process is non-trivial, and involves adjusting for parameters related to metallicity, total cluster mass, extinction terms, among others. The equation[4]:

$$t = \frac{M}{L} = \frac{M}{M^{3.5}} = \frac{1}{M^{2.5}}$$

can be used as an approximation for the cluster age, as it is an estimate of stellar lifetimes in terms of the life time of the sun (~10 Giga-years) and solar masses. Simply computing the age of the stars at the turnoff point can yield a rough estimate of cluster age. This technique for calculating age based off the HR diagram is unique to clusters, and is invaluable to parameterizing any age dependent phenomena.

Focusing on the main sequence, hydrogen fusion transfers energy to the outer layers of a star in two particular ways. The first, radiative energy transfer arises in areas where the opacity of the fluid is low, and temperature gradients are lower. These areas are known as radiative zones, and the chief way of transferring energy arises from photon-matter interactions.[6] Hydrogen fusion releases high-energy photons in the form of gamma radiation. These photons are scattered, absorbed, and reemitted a multitude of times by the stellar interior before being emitted at the surface.

In areas where opacity is high, and temperature gradients are also large, energy begins to move by convection. In this case, the absorbed photons from fusion cannot move through the area at a rate fast enough to keep energy at a relatively even distribution within the plasma. This leads to the plasma redistributing itself as a way to reduce the temperature gradient.[9]

The size and location of the radiative and convective zones vary as a function of stellar mass. Figure 3 illustrates the variation in energy transfer.[10] Stars that are more massive have core convective regions and exterior radiative zones, related to the CNO cycle for hydrogen fusion being incredibly temperature sensitive and thus producing a large temperature gradient in the stellar interior. Solar mass stars have interior radiative zones with exterior convective regions.[9] Star spot studies are interested in the latter group because convective regions are necessary for spot formation.

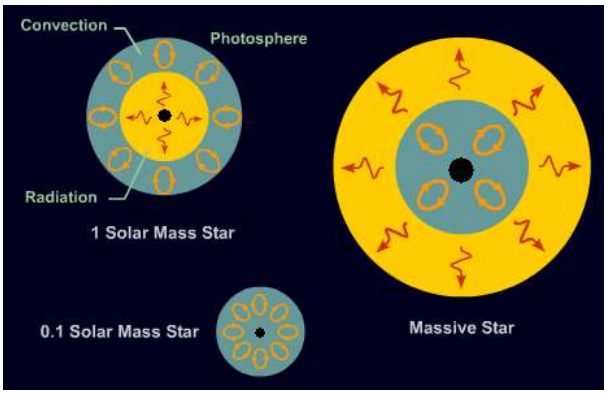

Figure 3: The radiative zones of Stars with varying masses[10]

Within the outer convective region of low mass stars, convection presents as granulation on the solar photosphere.[9] Granulation manifests as a bright central region of gases rising from the stellar interior, coupled with an outer dark region of cooled gas returning to the stellar interior (figure 4[11]). These regions are the result of Rayleigh-Bénard convection, which rises from uniform heating beneath the convective surface.[12]

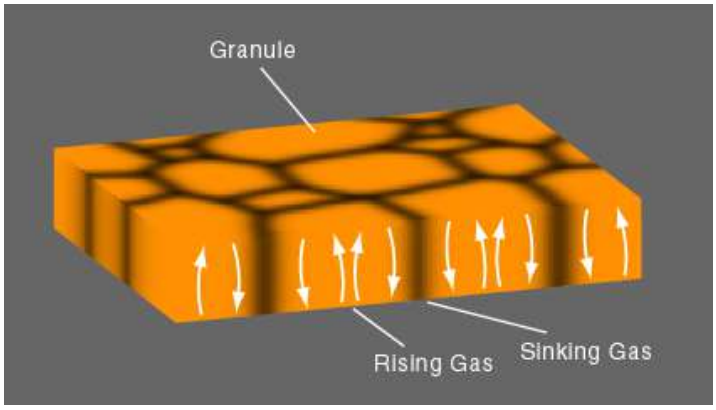

Figure 4: Granulation and Convection[11]

The convective zone is believed to be the source of the magnetic dynamo for dwarf stars. The exact nature of the dynamo is an area of active research (like this research) but the predominant theory follows from the fact that stars are composed of plasma, a state of matter denoted by a separation of charges into discrete regions.[13] The circulating motion of the plasma in the outer convective zone generates a net movement of charge in cyclical loops. The current loops give rise to local magnetic fields within the plasma. These fields superimpose to create the dipole field that is observed on stars.

The discrete nature of the stellar magnetic field gives rise to many of the magnetic phenomena of stars. Of primary interest are sunspots, a unique feature of several properties of these dwarfs. They arise from a combination of stellar rotation, and the convection induced magnetic field.[13]

The rotational nature of a star is quite different from a planetary body. Because it is a fluid body, it undergoes differential rotation with respect to latitude.[3] Physically, the rotation rate is a function of the total angular momentum of the system, the variation of

fluid density across the body, as well as the magnetic field interactions within the fluid. In nature, bodies undergoing differential rotation rotate more slowly at the poles than at the equator.[13]

The difference in rotational speeds causes sections of plasma that are part of the same dipolar field line to be stretched out across the surface. Over successive rotations, the individual field lines become entangled, puncturing the stellar surface, and disrupting convection.[2] Convective disruption causes the surface plasma to remain beyond the point when it should be thermally buoyant.[13] This plasma is cooler than the magnetically undisturbed plasma, and thus releases less radiative energy. The resulting loss of energy in that portion of the surface is known as a sunspot on the sun and as a starspot generally.[2] The model that describes field-line entanglement is known as the Babcock model. It likens field-lines to thread being wound up a spool and becoming intertwined as it does.[2]

The Babcock model also demonstrates an additional component of solar activity, the steady movement of sunspot locations from the poles to the equator.[14] starspot movement is dictated by the point of entanglement of magnetic-field lines. As the star progresses through its cycle, the magnetic field lines become more entangled, allowing sunspots to appear far more numerously, and in areas closer to the equator.[2]

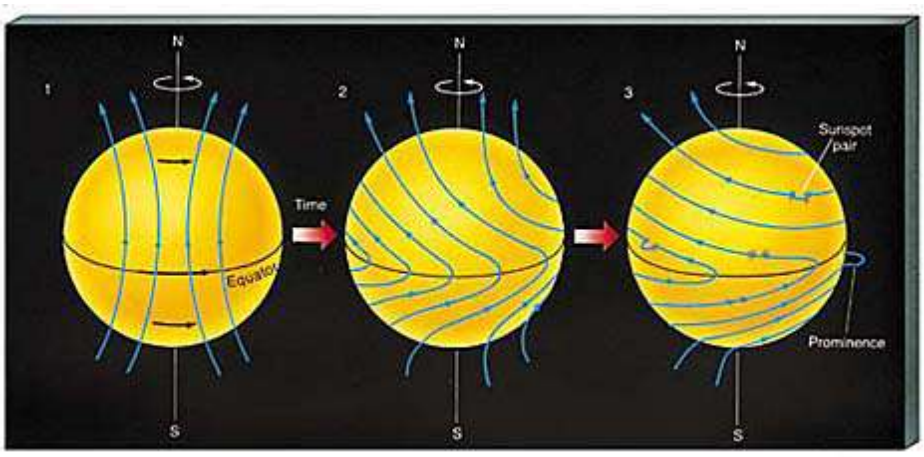

Figure 5: The Babcock Model of magnetic field motion[14]

This behavior is modeled in what are known as the Solar Butterfly diagrams.[2] These describe the apparent magnitude and location of each spot with respect to stellar latitude and time. There is a clear trend toward the equator with time, as well as a noticeable gap between each successive cycle. Additionally, starspots are symmetrically distributed across the equator, a direct result of the dipolar nature of the field and the symmetric nature of differential rotation.[2]

The entire activity cycle crosses two successive cycles of the butterfly diagram, accounting for the reversal of the magnetic field that occurs when the starspots reach the equatorial region. The exact nature of the reversal is a matter of active research, but the prevailing theory is that the level of entanglement reached when the starspots are occurring on the poles causes the dipole to reorganize itself into a lower energy configuration, which is more easily reached by reversing the magnetic dipole.

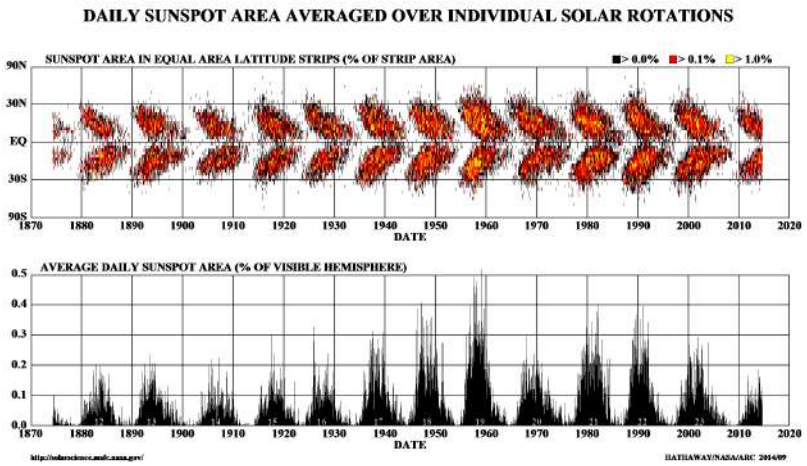

Figure 6: Solar Butterfly Diagrams spanning 1870-2014.[2]

These models are most readily applicable to the sun, where spot activity can be directly resolved and magnetic field strengths directly measured. On other stars, this process becomes complicated. It is impossible to directly resolve the airy disk of even the closest stars.[4] Without this, individual spots and spot locations cannot be directly determined from images.

Instead, physicists utilize the blackbody nature of the star, and the spots to detect surface spots. Because starspots are cooler than the surrounding plasma, they produce a lower flux than a similar area of plasma at the T_{eff} of the star. This can be observed as an apparent dimming of a star that has a starspot in the line of sight of the observer. Stellar dimming can be quantified utilizing CCD images. These images have a count value recorded with each pixel, with each count corresponding to an incident photon from the stellar source.[15] Because counts scale linearly with incident photons, they can be considered an analog of flux and utilized to determine the apparent magnitude of the source with the equation[4]

$$m_B - m_A = -2.5 \log\left(\frac{F_A}{F_B}\right)$$

where $m_B - m_A$ is the difference in magnitude between two objects, and $\frac{F_A}{F_B}$ is the flux ratio of those objects. In practice, only the instrumental magnitudes are needed for photometry, and m_B is defined as the zero-point of the frame, with a flux of one.[16] This reduces the equation to:

$$m_A = 2.5 \log(F_a)$$

which is defined as the instrumental magnitude, and used for all calculations.

As the star rotates, the starspot will follow the rotation, bound to the local magnetic field. For stars with an axis of rotation reasonably close to perpendicular as viewed from earth, the starspot will appear to transition across the stellar surface and then rotate behind the star.[2] Once the starspot has moved behind the star, the apparent magnitude of the star will increase, bolstered by the increase and flux caused by more of the surface radiating at T_{eff}. [17]

This rotation also modulates the brightness periodically, fitting a sinusoid of the form

$$\phi(t) = Asin(\omega t + \varphi)$$

Where ω is the angular frequency, which can be used to define the period

$$T = \frac{2\pi}{\omega}$$

which is the rotational period of the star. Variation in the rotational period as the starspots transition to areas of increased rotational speed can be used to construct the cycles present in the butterfly diagram, and thus build the activity cycles of these stars.[2] That topic is not dealt with in detail here. Instead, the focus is on the ability to precisely measure the periodic variations of these stars due to spot activity, and the magnitude of these variations.

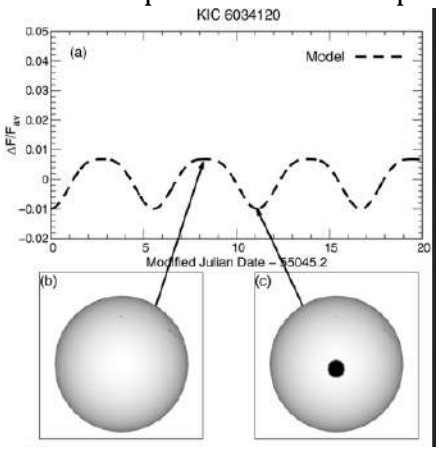

Figure 7: Model of Lightcurve and depiction of rotating starspot[17]

Experimental Methods and Data Acquisition

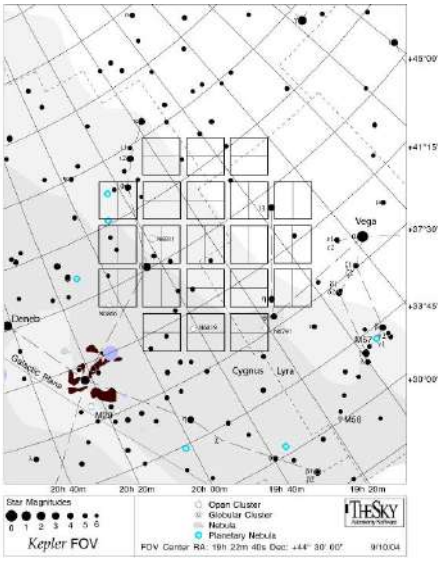

Figure 8: The Original Kepler Field on a Star map. Each rectangle corresponds to the field of view of an individual CCD chip.

The initial push for working with NGC 6811 came from the recent launch of the Kepler planet hunting satellite. Kepler offered near continuous photometric observation of thousands of stars within a 105 square degree section

of sky.[18] This field is located on a region extending upward from the galactic plane, and within this field were several open clusters of varying ages.

Of these clusters, NGC 6811 Proved to be particularly interesting for a number of reasons: It was older than previous clusters examined by Gettysburg, but still younger than our sun. NGC 6811 had a calculated age, and sufficient radial velocity measurements to identify members with accuracy.[19] There were also previous images of NGC 6811 within the Gettysburg observatory files taken in 2007. Additionally, it was the subject of a gyrochronology study by Meibom et al.[19] The Meibom study examined stars with identifiable rotational periods, which they deduced to be from spot coverage. These stars, along with the rotational periods and magnitude information were reported in the paper, and form the basis of this viability study.

Figure 9: The 0.4m Cassegrain at GCO

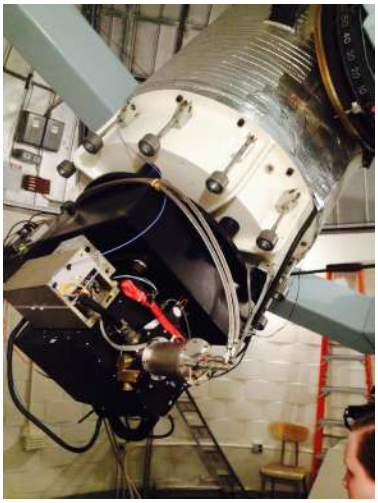

Figure 9: The CCD and Optical Tube of the 0.8m at NURO

Data was collected using three different instruments on three different time scales. The oldest dataset collected utilized the Gettysburg College Observatory. The observatory is equipped with a 0.4-meter Cassegrain telescope with a liquid nitrogen cooled CCD. The data was collected on various nights from May to October 2007. The images were centered on the accepted center of the cluster RA 19:37:19.9 and Dec

46:23:17, and exposed for 240 seconds each. Images were taken in the I and V Johnson filter bands. Logs do are not available for these images, so it is difficult to say anything about telescope focusing or other conditions present in the telescope that may effect the images. Calibration frames in the form of Bias, and dark and flat-field frames were taken at the beginning of the night.[16]

The other ground-based datasets were collected at Lowell Observatory using the 0.8-meter National Undergraduate Research Observatory telescope, and the NASACAM CCD. These data were taken over the course of June 21-24 2013 and June 22-25 2014. The 2013 data was taken through Johnson BVR filters[20], for 300 seconds. The filters were taken in rotation with one image per filter per cycle. 300-second BVR frames were taken on the first night of the 2014 observing-run, but the R filter was later omitted in an attempt to increase the number of observations as NGC 6811 and NGC 6866 were being observed concurrently. Focusing of the telescope was performed every 90 minutes in 2013 and every 60 minutes in 2014. Bias and flat-field calibration frames were taken in 2013 and 2014. Additionally, dark frames were taken at the beginning and end of each night in 2014 to compensate for the CCD running hotter than standard operating temperature.

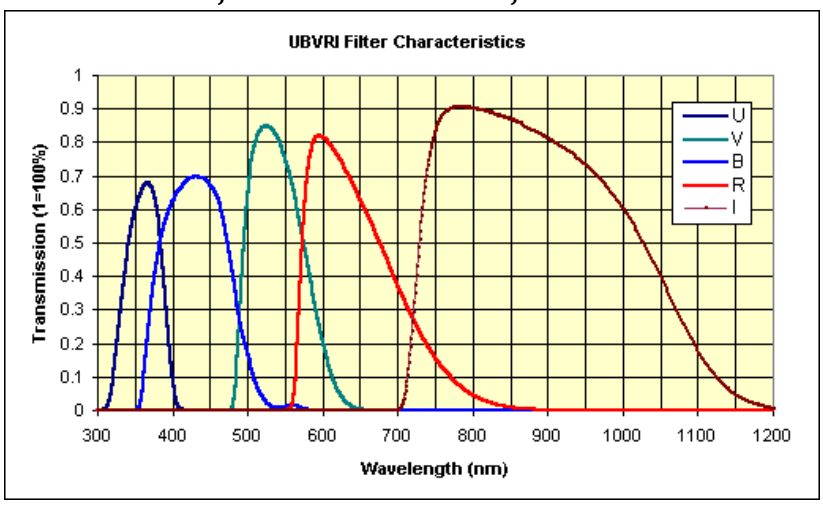

Figure 10: The Johnson Filter Passbands[20]

Images were calibrated to reduce instrumental contamination, particularly CCD contamination, using calibration frames. The three major types of calibration frames are

Bias, flat field, and dark frames. Each one of these operates on the frame containing the images, the science frame to remove some element of noise.

Bias frames are a zero second exposure of the CCD that examines the threshold level of counts that are always present in the CCD along with the readout noise from the CCD. Twenty-five bias frames were taken and median combined to find an average value for the counts across the CCD. The averaged bias frame is subtracted from all the other calibration frames, as well as the science frames before any further calibration occurs.[15]

Dark frames are similar to bias frames. Darks are an exposure of the CCD with the shutter closed for the length of the longest science exposure. This allows for isolation of the thermal noise of the CCD that is collected over the course of the exposure. The dark frames are median-combined to create an average frame representing the thermal noise across the CCD for the exposure length. CCD thermal noise is treated as linear, so the Dark frames are bias-subtracted, scaled to the exposure length, then subtracted from the science and flat-field frames.[15]

Flat-field frames are the final calibration frames. These are 1-second exposures of a uniform field of sky. They are taken at either dawn or dusk, in a location 90 degrees from the sun. The purpose of a flat-field frame is to quantify the CCD response across the entire chip, and compensate for non-uniform responses. Flat-field frames are median combined as well as dark and bias subtracted. The master flat-field frame is then normalized by the median value. The science frame is divided by this normalized flat-field to remove the variation that arises from the non-uniform CCD response. The entire data reduction/calibration process follows the equation[15]

$$Science_f = \frac{Science_i - Bias - (Dark - Bias)}{Norm(Flat - Bias - (Dark - Bias))}$$

for the ground-based images. The 2007 images were previously processed and retrieved from the GCO archive. The 2013 and 2014 images were processed utilizing *ccdproc* in IRAF v2.16 and following the method outlined above.

Figure 11: The Kepler Satellite[21]

Data from the Kepler archive were taken with the Kepler Satellite. The satellite contains a 1.4-meter primary mirror with a 42-chip CCD array located at its prime focus.[21] Unlike the ground-based observations, Kepler is unfiltered, and thus Kepler photometry records signals across the entire dynamic range of the CCD, which spans 400-900nm.[21] Kepler collected NGC 6811 data in long-cadence intervals, which means the CCD was exposed and read out in 29.4-minute time steps. These time steps were complied into a single *.fits* file and transmitted to earth at the end of every 31 day observing quarter.[22] Initially, every portion of the Kepler FOV was

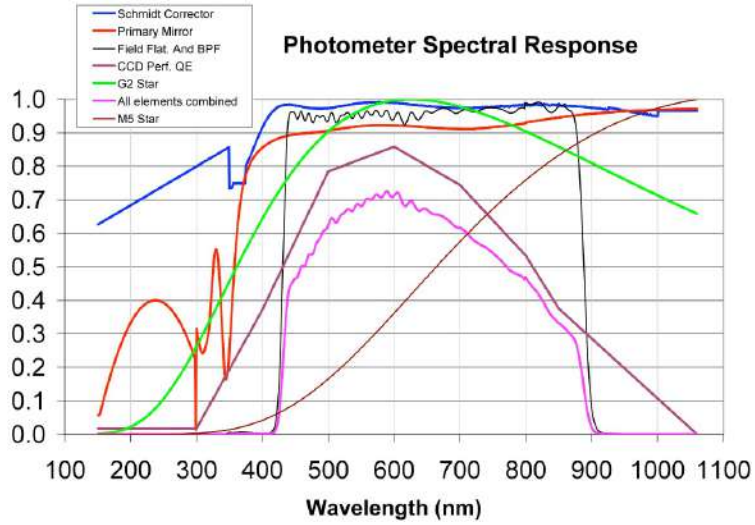

Figure 12: Kepler Spectral Response. The Pink curve is the total response of the system.[21]

observed in each quarter, but this became impossible after the failure of a section of the CCD. As a result, Kepler was rotated every quarter to reposition the failed section, meaning objects that would have focused onto that section are lost in that quarter.[21] All data for the selected stars that is available within The Kepler archive was retrieved for rotational period examination.[23] This extends from May 12, 2009 to May 11, 2013 at which point the second of Kepler's four reaction wheels failed and the spacecraft became unable to accurately track the Kepler FOV.[21]

Unlike with ground-based observations, Kepler data was not recorded as a single frame as this would make excessive memory demands, and result in large quantities of empty space being recorded.[23] In order to maximize the efficiency of each quarter, Objects of interest were defined with an aperture mask.[22] The aperture mask defined a statistical region that maximized the signal of the object with respect to contamination from the CCD and the surrounding field. These aperture masks and the raw counts from within these masks were recorded by the mission and returned to earth as what are called *Target Pixel Files.*[22] All analysis performed on Kepler data utilizes these Target Pixel Files as a starting point.[23]

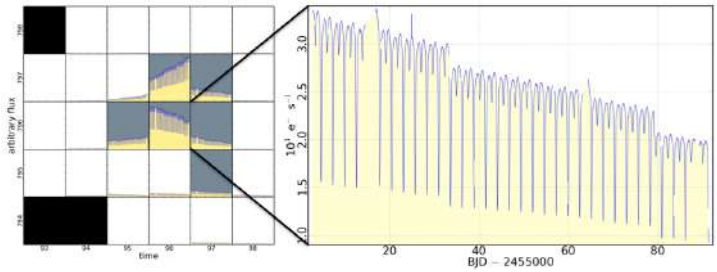

Figure 13: An example of a Target Pixel File, and a visualization of how lightcurves are extracted from these files.

Rotational stars were identified in a VizieR catalog, and their positions were overlaid onto a Sloan Digital Sky Survey image of the cluster using Aladin. This image was then aligned with the images taken at the GCO in 2007 to determine which of the rotational stars were within the frame of the image. Additionally, selection was limited to objects that had not been examined by

students in the previous year. This excluded the seven most luminous stars from further study. Magnitudes were further constrained by looking at stars near to $m_v \sim 14$ because stars of this visual magnitude at the cluster distance would be similar in mass and luminosity to the sun.

One final parameter of selection was set in whether the stars could be identified as single members of the cluster. NGC 6811 lies in a region that is saturated with field stars. This means that stars unassociated with the cluster are in our line of sight, and obstructing it. Because of this, it is imperative to separate stars within the cluster from field stars, so the cluster aging method can be utilized. If the stars measured were not in the cluster, star aging becomes much more complicated and imprecise, and the data for that star would not be useful for defining the parameter space of rotating cool dwarfs.[7] For this reason, only stars claimed as single members by *Meibom et al*. were chosen. Having established these selection criteria, each researcher selected three stars. The three stars presented are listed in table 1, and include all rotational values reported by *Meibom et al*.

Name	Rotational period	Coordinates (RA, Dec)	V-band Magnitude	Color Index B-V
KIC9655315	$10.85 \pm 0.35\ days$	19:37:14.4 46:22:14.3	15.23	0.65
KIC9715987	$10.27 \pm 0.58\ days$	19:36:45.33 46:27:15.7	15.33	0.739
KIC9716650	$11.08 \pm 0.37\ days$	19:37:45.97 46:27:30.3	15.34	0.681

Table 1: The Candidate Stars

The method employed for examining brightness variations is known as photometry. Photometry examines the change in flux of a target star with respect to time. Photometric methods must be able to correctly separate source variation from variations induced by turbulence and uncertainty in the atmosphere or instrumentation. The instrumental

uncertainties arise from the reflectivity of the optics of the telescope being wavelength dependent or from the detector having a wavelength dependent quantum efficiency.[16]

Atmospheric variations are the result of air not being a uniformly transparent medium. The overall transmission of light through that atmosphere is dependent on the amount of air, or airmass, between the object and the detector.[16] Airmass is a function of the zenith angle, increasing proportionally to the secant of that angle, and is used to define the primary extinction term.[16] Primary extinction affects all stars equally, and presents as an overall dimming of the field of view as higher airmasses are approached. An additional term, secondary extinction deals with transparency variations as a result of color. The color term arises from Rayleigh scattering, and is dependent on the zenith angle, with the effect of the scattering becoming more pronounced as larger airmasses are reached.[16] Multiple methods for determining flux variations from targets exist, two of which are utilized in this paper. The first was utilized on ground-based observations from the GCO in 2007 and the NURO observatory in 2013 and 2014.

Photometry of ground-based observations made use of differential photometry. Differential photometry is a method of determining target flux by calculating the number of counts on the CCD within a defined aperture of pixels.[15] This aperture is defined by calculating the Full Width Half Max of the source, and setting an aperture diameter equal to double the

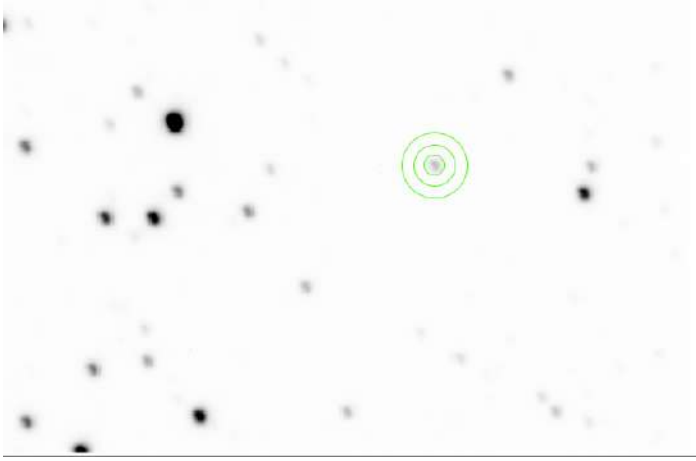

Figure 14: An example aperture around KIC9715987

FWHM.[16] An annulus of apparently empty image is defined around the source, and used to correct for any signal that is present in the background of the sky. This annulus is defined as containing a pixel area three times that of the target aperture. The counts are converted into a count rate, multiplied by the total number of pixels within the target aperture, and then subtracted from the target aperture.[15]

Differential photometry then seeks to remove the atmospheric and instrumental variations present by defining a reference point within the image that exists with a known flux. This allows for quantifying the variation induced by external forces.[15] The reference point is commonly a comparison star. The comparison star in differential photometry is located within the same field of view as the target star so that the difference in airmass between the location of the comparison star and the target small is negligible.[16] This is to keep the primary and secondary extinction terms uniform. The comparison star is placed in an identical aperture to the target star, and background subtracted in the same manner.[16] An additional star, called a check star is treated in the same manner as the comparison star, and used to verify that the comparison star is constant.[16]

The comparison star is subtracted from the target star to remove the instrumental variations. For this reason, it is imperative that the comparison star be similar in magnitude and color to the target.[16] A star that is much brighter than the target will extend beyond the ideal aperture defined by the target FWHM and lead to a loss of comparison signal. A color variation would cause a systematic variation in the light incident on the detector due to secondary extinction, and would become apparent if the comparison star had a spectral density peak that was far from the peak of the target star, and result in the reference point not accurately describing the target.[16] The check star must be selected in a

similar fashion to the comparison star, as it must fit within the defined target aperture and must experience extinction values identical to those of the comparison and target stars.

The odds of having a comparison star, or a comparison and a check star with identical magnitude and color values within the target FOV are very low, so allowances must be made. Magnitude is generally the more important parameter to match as the narrower passbands of the filters limit the effects of secondary extinction. Color is still important in a relative sense, as stars with peak emissions at opposing sides of the passband can continue exhibit secondary extinction discrepancies even within the filtered light.[16]

Comparison stars were selected from the listing provided by the American Association of Variable Star Observers.[24] A similar method of identifying comparison stars in the GCO images was employed. A star map was generated on the AAVSO webpage and the map was aligned with the GCO frame for stellar identification. Candidate comparison stars within the frame were then compared to the selected rotational stars to determine similarity of V band apparent magnitude, and the B-V color index and are listed in Table 2. These stars represent the reference stars of closest magnitude and color to the targets available within the telescope FOV.

Name	Coordinates (RA, Dec)	V-Band Magnitude	Color Index (B-V)
000-BCT-308 (Comparison)	19:36:59.5 46:19:07	14.013	0.797
000-BCT-310 (Check)	19:37:17.8 46:19:07	13.817	0.469

Table 2: Photometric Comparison stars

Differential Photometry was handled by *MIRA-7* software. The images collected over the course of a night were imported into MIRA and examined using the photometric software package. Full Width Half Maxes for each star were determined using the Statistics package, and the aperture and annulus were defined according to this value. The widest FWHM for a given star on a given night was taken, and each target star was examined individually to maximize the SNR by selecting the optimal aperture for each star.[16]

Photometric analysis of the Kepler data also utilizes differential photometry as a means of quantifying variations in the apparent flux of the target star. Its execution varies from ground-based methods in a number of ways. First, Kepler only records the fluxes of stars with photometric significance as a method of preserving memory space between transmissions.[22] This means that all Kepler objects are photometrically active and unusable as reference points for other Kepler objects.[22] Light incident on Kepler is also unaltered by atmospheric effects, being an orbital telescope. Because of this, Kepler analysis need only take into account the variation introduced by the instrument itself when attempting to quantify the variation of the object.[23]

For this reason, Kepler records the values of several pixels located across each of the detector modules. These pixels correspond to empty space, and the random fluctuations of the CCD and the system are recorded in the flux incident on these pixels. These pixels are compiled and denoted as *cotrending basis vectors*[23]. Within the Kepler data reduction pipeline, these vectors are subtracted from the summed flux of the pixels within the ideal aperture mask of the target pixel file in such a way that the SNR of the target is maximized.[23] Additional error reduction is performed within the data reduction pipeline in the form of baseline lightcurve signals, which are compared to the raw lightcurves

extracted from each target pixel file and used to identify places of potential contamination from pixel read errors or other electronic failures.[22]

Lightcurve data can be taken directly from the archive having already been processed using the Kepler pre-search data conditioning pipeline. It can also be extracted directly from the target pixel files utilizing the *PyRAF* package *PyKE* to perform the tasks of the pipeline including defining the ideal aperture mask, and applying the cotrending vectors.[23]

Lightcurves from both ground-based and Kepler observations are created by plotting the total number of counts within the target aperture after the photometric processing has taken place with respect to the heliocentric Julian date of the start time.[16] Julian date is a running count of the number of days since the beginning of the Julian calendar. It is used in astronomy to define a continuous timescale long enough for astronomical phenomena to occur, unlike the modern calendar, which involves a cyclic progression of days and months.

The lightcurve data were fed into *Peranso,* a period-finding program that is equipped with a Fourier-based method for determining periods when data is incomplete or spaced over large regions of time. This routine is called a Lomb-Scargle periodogram.[25]

The Lomb-Scargle periodogram operates by defining a periodogram similar to the one used in Discrete Fourier Transforms. Lomb and Scargle arrived at the same function from two different methods. Lomb sought to use Least Squares to minimize the sum of squared residuals of the fit of a linear combination of sine curves onto the data, while Scargle utilized statistical inference to modify the existing discrete periodogram for evenly spaced time intervals. These methods produced a coincident result, one defining the

minimization of Least Squares, the other defining the periodogram, but both utilizing the same equation[25]:

$$P_x(\omega) = \frac{1}{2}\left[\frac{\left[\sum_j \cos\omega(t_j - \tau)\right]^2}{\left[\sum_j cos^2\omega(t_j - \tau)\right]} + \frac{\left[\sum_j \sin\omega(t_j - \tau)\right]^2}{\left[\sum_j sin^2\omega(t_j - \tau)\right]}\right]$$

where τ is a constant used to maintain a phase independent periodogram, as found in Discrete Fourier Transforms, and is defined as:

$$tan2\omega\tau = \frac{\sum_j \sin2\omega t_j}{\sum_j \cos2\omega t_j}.$$

The periodogram is applied computationally by defining a step size for ω and solving the periodogram equation for each step from a generated starting point. *Peranso* defines the value of the periodogram for a given frequency as *theta.*

Analysis

The 2007 observations are the oldest of the datasets, as well as the most problematic. The GCO telescope was plagued by tracking issues in the area approaching and receding from the meridian, a position the cluster occupied for many of the observations. This is evident in star trails, and doubling of stars in the field for many of the frames. Additionally, the focus in many of these frames was quite poor, especially in the latter half of the spring and summer observing sessions.

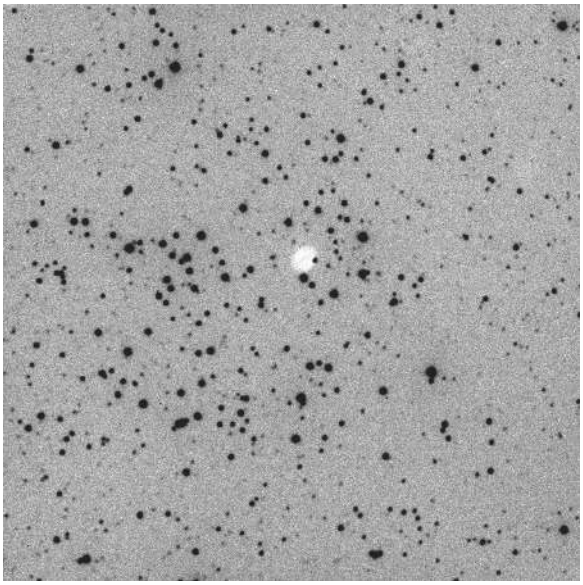

Figure 15: frame from the 2007 dataset

Because of these irregularities in the frames, the FWHM of each star was significantly wider than it would have been under ideal

tracking and focus conditions. Among many other things, this greatly lowered the SNR of the target and increasing the error in the calculated magnitude. The SNR was calculated using the following[16]

$$SNR = \sqrt{\frac{N^*}{N^* + n_{pix}N^{Sky}}}$$

where $N^*$is the number of counts for the source object, n_{pix} is the number of pixels within the source aperture, and N^{Sky} is the number of counts per pixel within the background annulus.

This error is compounded by the error in the reference stars, which must be added to the error of the target star in quadrature. *MIRA* calculates magnitude error as the standard error of the pixel distribution within the target aperture. The lightcurves for the 2007 observations (T-C) along with the lightcurves of the variation in the reference stars (C-K) are presented in graphs 1, 2, and 3. These reflect the variation between the comp and check star for every frame. It is worth noting that the variation between both the target and comparison star and the comparison and the check star vary on the order of nearly 0.5 magnitudes in the course of a night. This variation, without even considering the associated errors, would completely mask any variation due to spot activity.

In spite of this, the lightcurves for each target minus comp, and each comp minus check were still examined with Peranso to see if there was any periodicity that could help understand the massive variations over the course of a night. The parameters for Lomb-Scargle were set to scan periods ranging from two days to 80 days, with a resolution of 3000. The lightcurves were not particularly illuminative in this case.

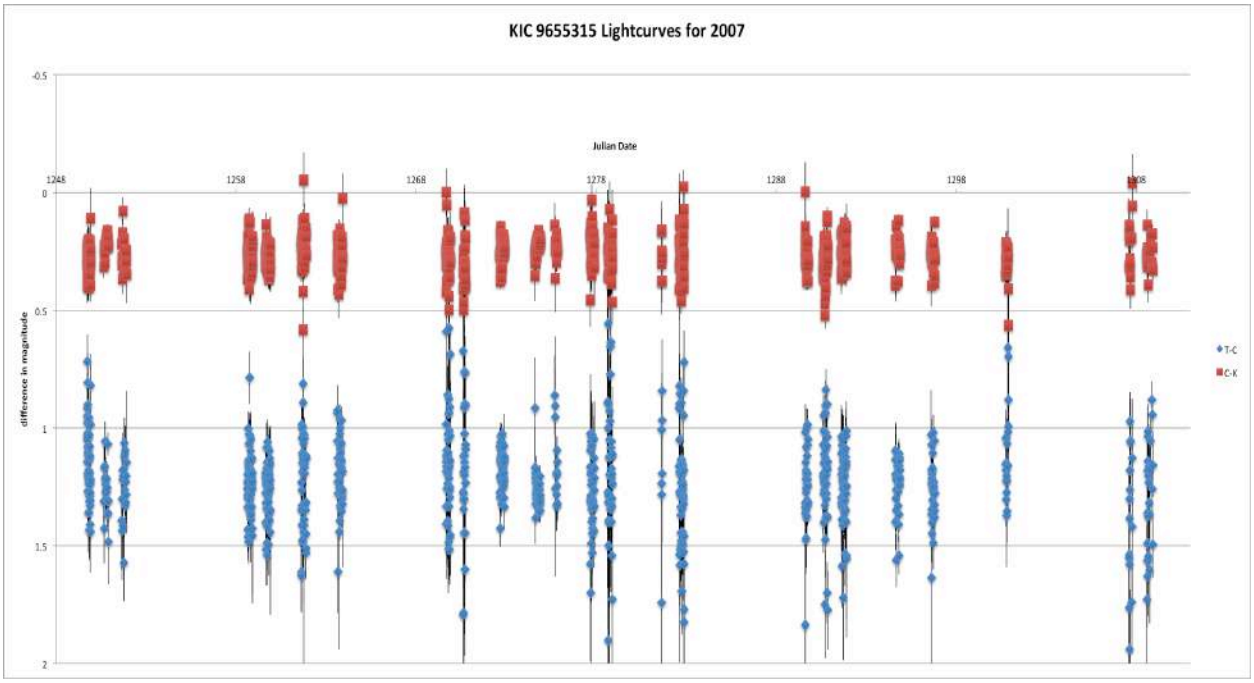

Graph 1: KIC9655315 lightcurves from the 2007 GCO data

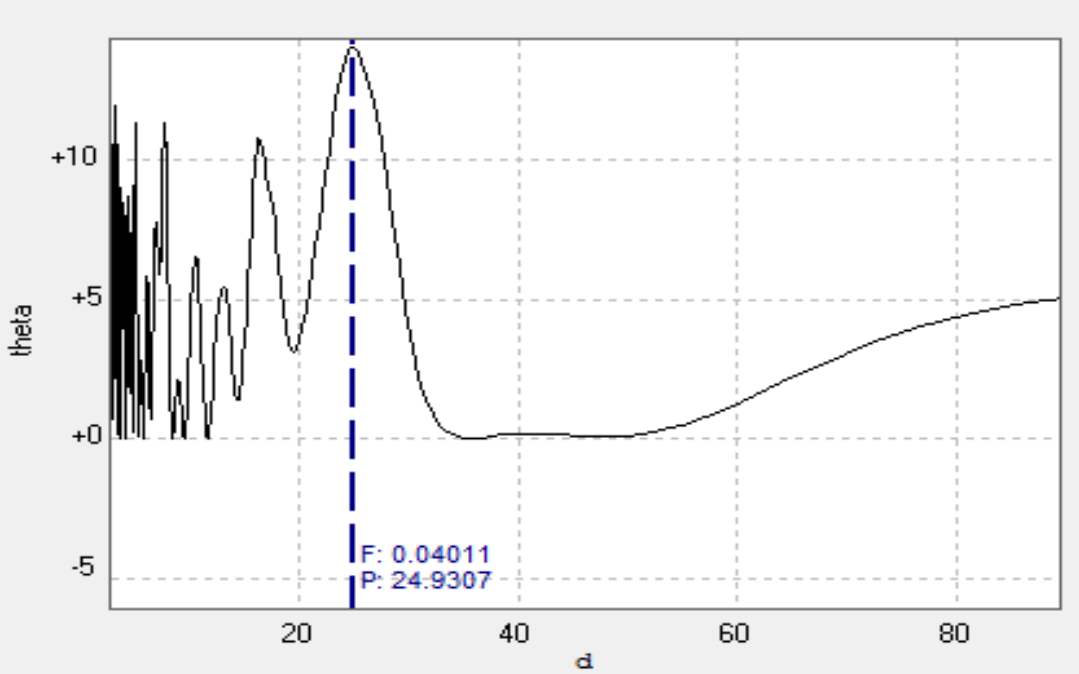

Figure 16: the T-C lightcurve periodogram of KIC96655315. Note aliasing at 24 hours

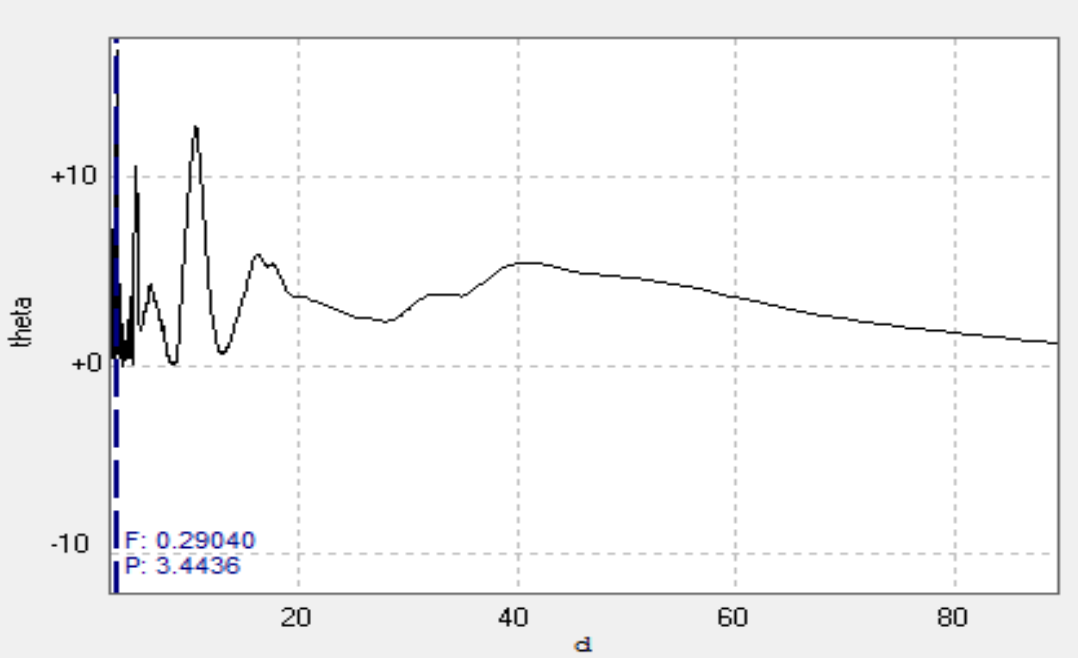

Figure 17: C-K lightcurve periodogram for KIC9655315 in 2007

KIC9655315 exhibits some periodicity, but the dominant mode is near 24 days, which appears to correspond to the spacing between successive observing runs. There are other peaks with a large periodogram value, but these appear in an area where large peaks

occur in the C-K as well. Ideally, the C-K should not have any variation, which makes all periods located on the T-C, especially those very close to the periods of the C-K, suspect.

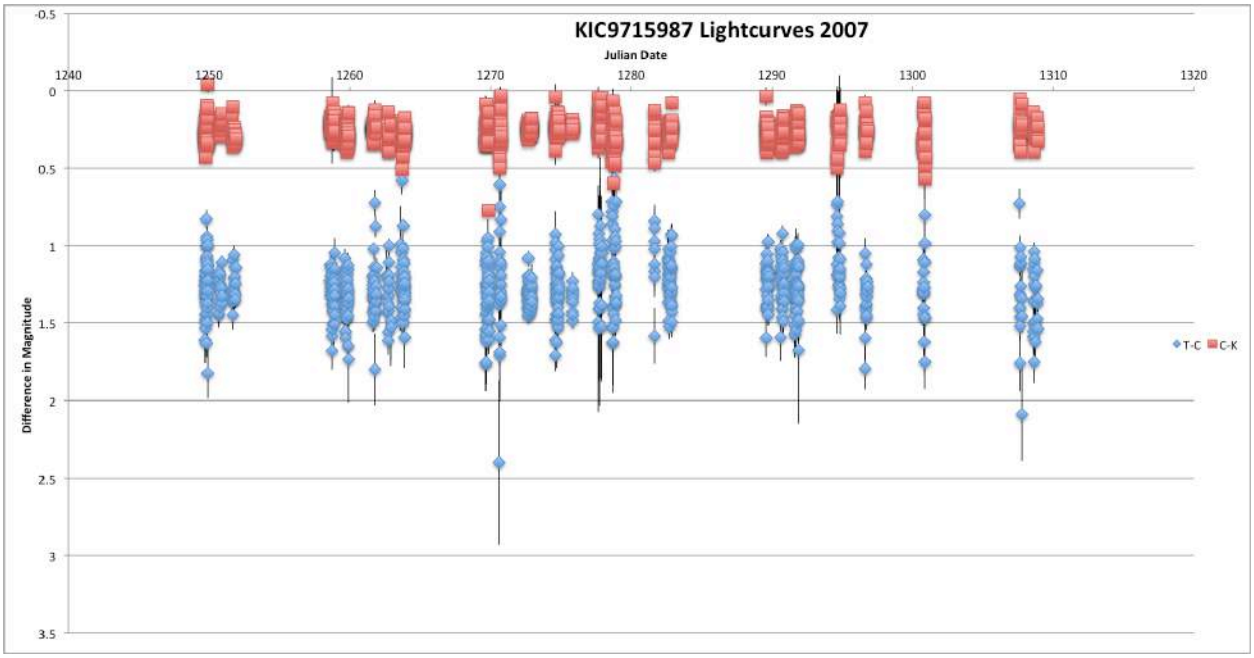

Graph 2: KIC9715987 T-C and C-K lightcurves 2007

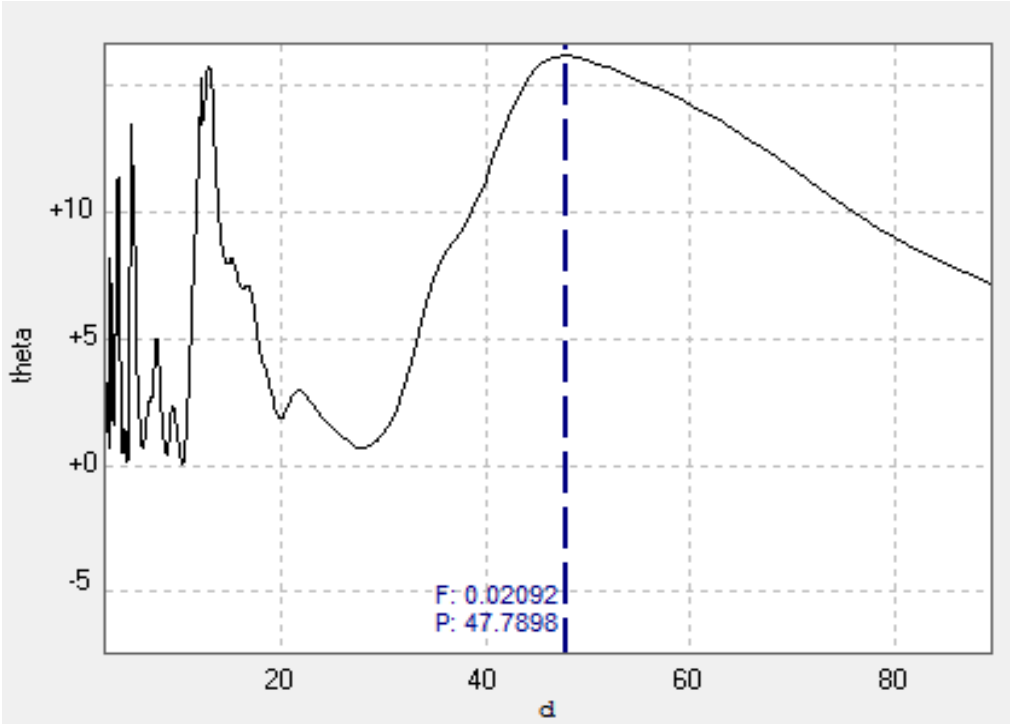

Figure 18: T-C Periodigram for KIC9715987 2007

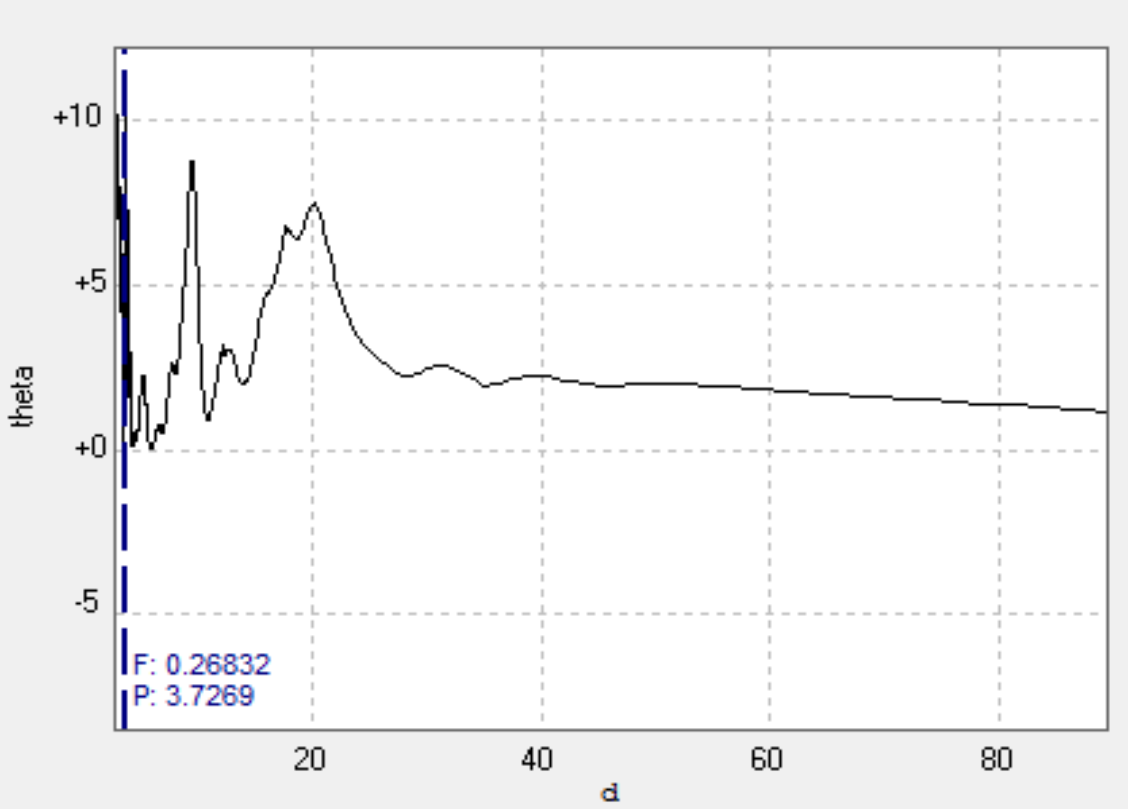

Figure 19: KIC9715987 C-K periodogram 2007

KIC9715987 also exhibited a dominant peak that appeared to be the result of windowing from the observational schedule. The T-C periodogram saw a peak at 48 days, or roughly two days. The C-K also sees a large peak near 20 days. T-C also exhibits a peak near 11 days, which does not seem to be matched by any peaks within the same region on the C-K. This peak is in line with what Meibom et al. reported for KIC9715987, and is also in line with what was extracted from the Kepler data. Having said that, the noise in the data and the other peaks within the periodogram make it impossible to say if this is a true rotational period, or simply a byproduct of the noise. The dominant period in the C-K likely comes from the large nightly variation seen in in the lightcurve.

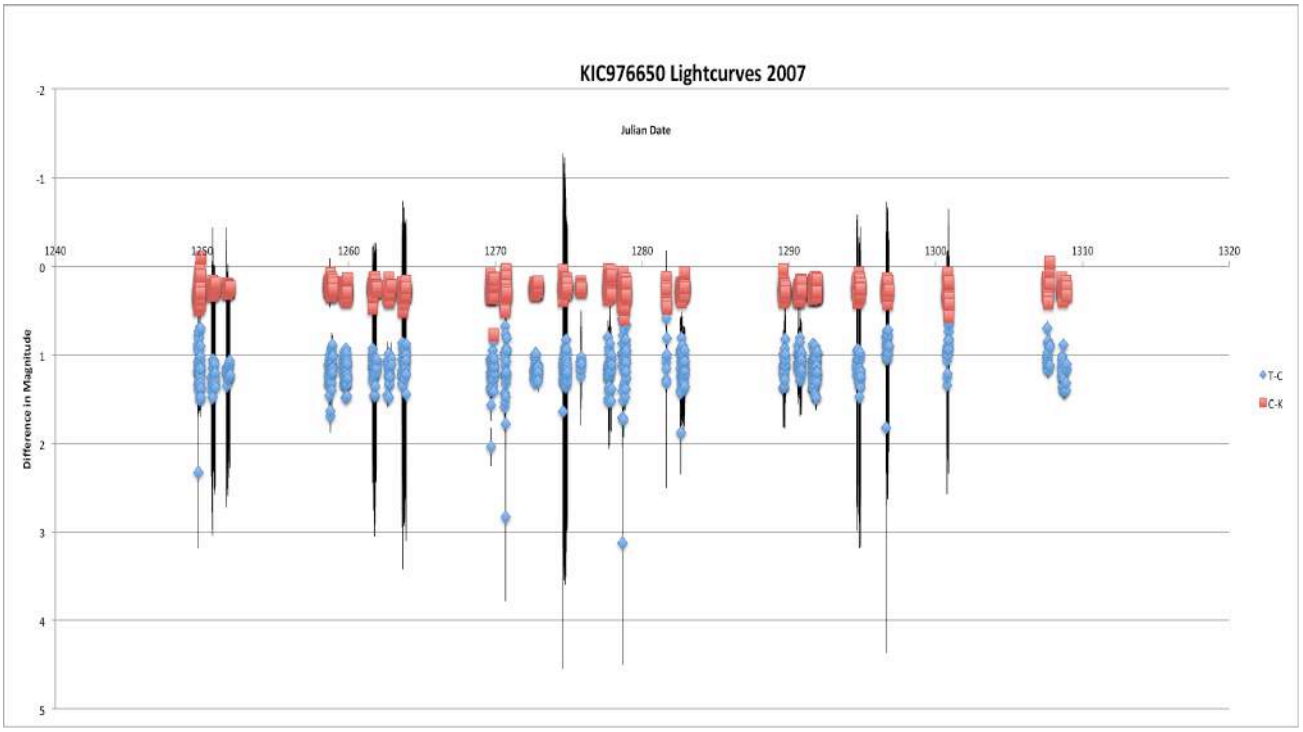

Graph 3: KIC 9716650 T-C and C-K lightcurve 2007

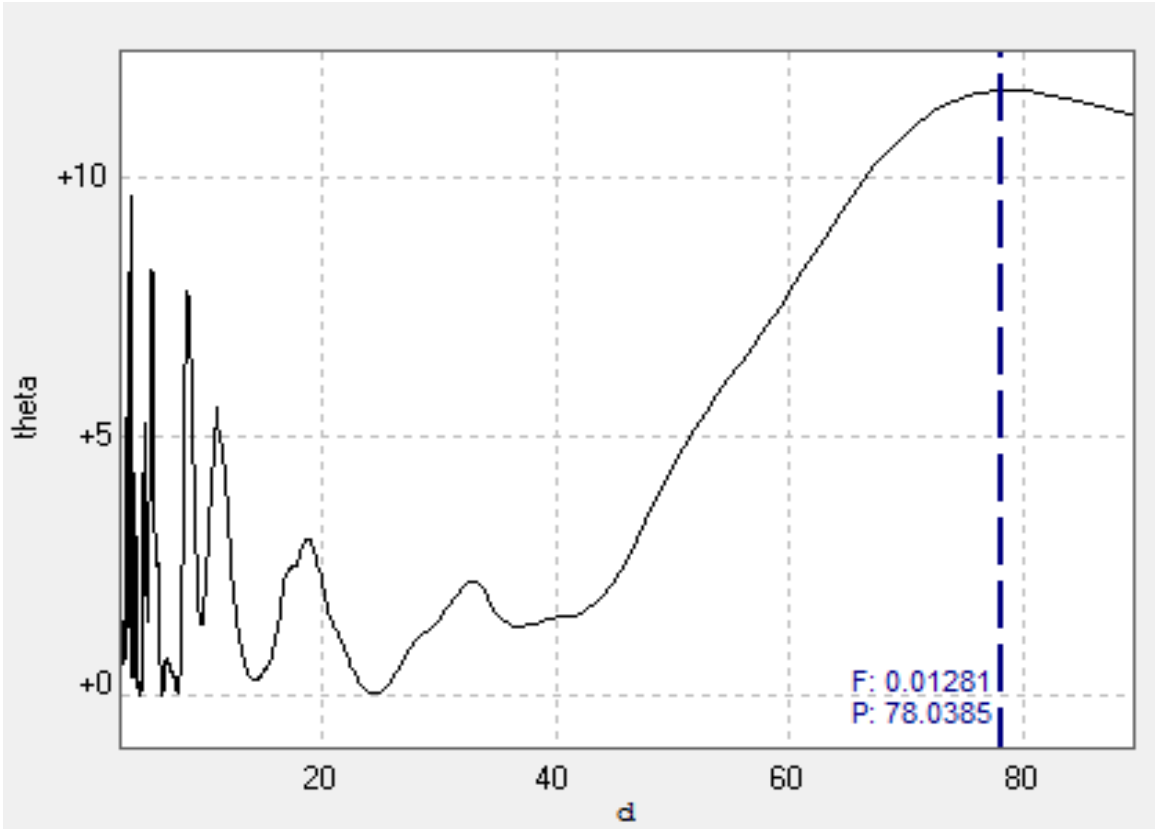

Figure 20: KIC9716650 T-C periodogram 2007

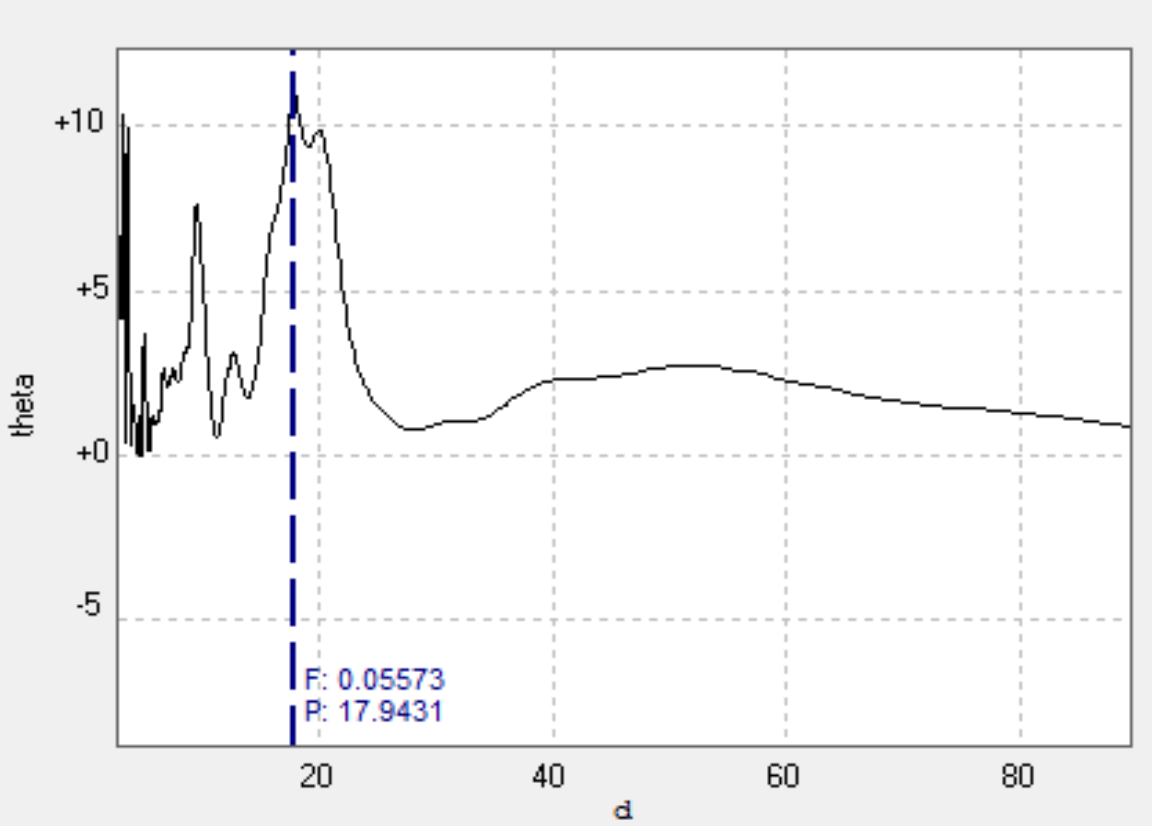

Figure 21: KIC9716650 C-K periodogram for 2007

KIC9716650 showed the lowest amount of periodicity among the three candidate stars. The largest period existed out near 78 days, which is about the length of time over which the data was collected. There are additional peaks between 3 and 20 days, but these peaks are weak in comparison to the peaks in the C-K periodogram. KIC9716650 had an additional source of error in the form of a nearby field star. When the FWHM of the stars was particularly large, a field star would expand and make it difficult to define a sufficiently large sky annulus, and would affect both the sky reading and the SNR of the target star, which is why the error bars on some data points are quite large.

The variation within the 2007 data resisted explanation due to the large errors associated with the quality of the images. 2013 and 2014 data taken at NURO presented

higher precision data and allowed for more accurate photometric measurements to be taken. The lightcurves were extracted using the same technique described for the 2007 data, and utilizing the same reference stars. Each observing run was only four days long so the data are presented together for ease of explanation. The T-C and C-K lightcurves are presented in graphs 4-6.

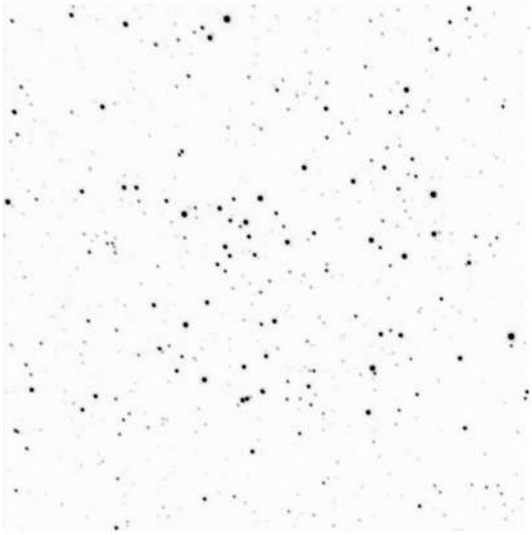

Figure 22: Frame from the 2013-14 dataset

None of the light curves exhibited any periodicity that could not be explained by windowing due to the shortness of the observing sessions. The reason for this may be related to the sparseness of the data compared to the length of time observed. There may be another reason for this, however. Both 2013 and 2014 data exhibit a unique form of nightly variation between the T-C and C-K values. Over the course the night, the variation of the two light curves seems to exactly mirror each other. The fact that this is occurring seems to indicate that there is some disparity in color between the comparison star and the target star.

The comparison star was the closest star in magnitude and color to the rotational candidates. This star is still noticeably bluer than the targets, as noted by the color index recorded in table 2. This color variation may be allowing secondary extinction to selectively dim the comparison star, shifting the reference point and making the target star appear brighter.

There is a simple solution to this issue. By determining the transformation equations of the telescope, a secondary extinction correction can be applied to the target

and reference stars to remove this source of potential error. Unfortunately, this requires photometric data from a pair of reference stars known as a red/blue pair. These stars are tracked through a range of airmasses, and used to correct for both atmospheric extinction and telescopic insensitivity. The measurements must be made concurrently with the observations to accurately correct for atmospheric discrepancies, which are the issue here, so the correction cannot be applied to current data, but it could be made to future observations.

The Kepler data was the most extensive of the datasets. It was also the most viable of the sets. Initial efforts re-extracted the lightcurves from the target pixel files and applied the co-trending vectors manually. These results produced lightcurves that could not be distinguished from the PDC lightcurves within the Kepler archive. Therefore, it was more advantageous to use the periodogram on the PDC data. The lightcurves for selected quarters for each star are presented below, and the remaining lightcurves are presented in the **Additional Lightcurves** section.

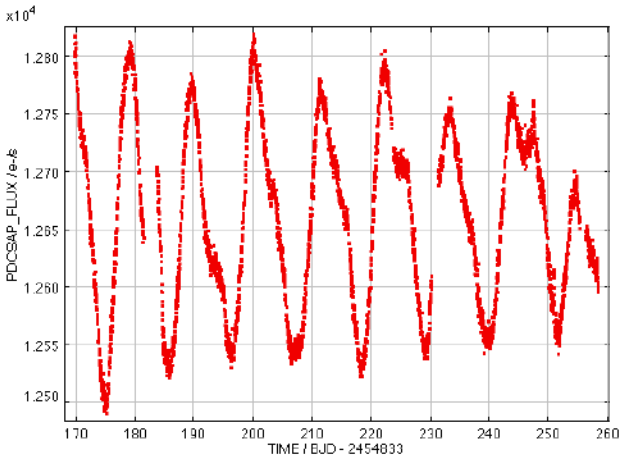

Graph 4: Lightcurve for KIC9655315 Quarter 1

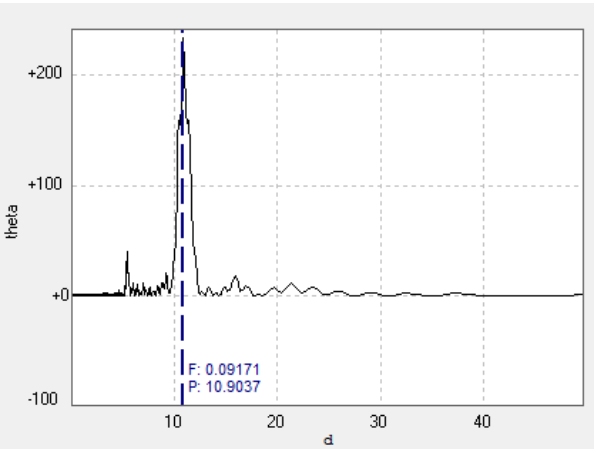

Figure 23: Periodogram of KIC9655315 Quarter 1

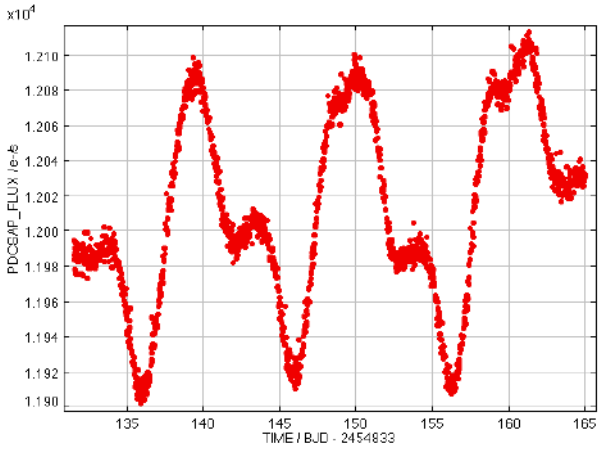

Graph 5: KIC9715987 Lightcurve for Quarter 1

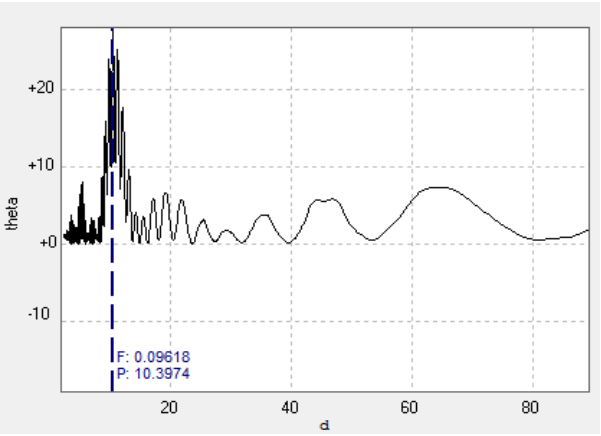

Figure 24: Periodogram of KIC9715987 for Quarter 1

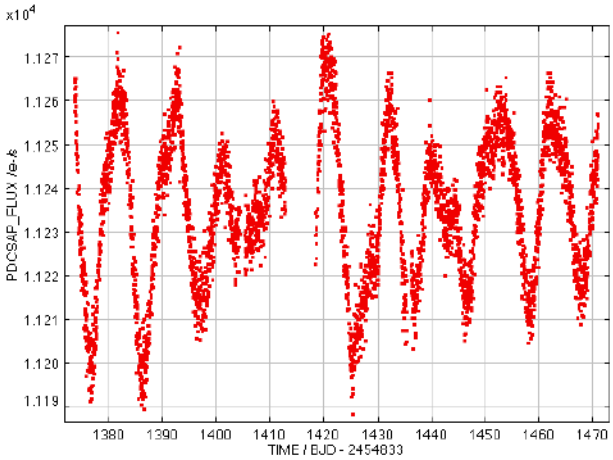

Graph 6: KIC9716650 Lightcurve for Quarter 16

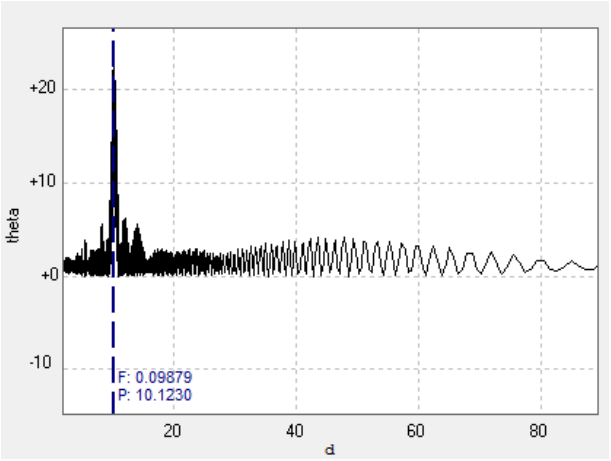

Figure 25: Periodogram for KIC9716650 for Quarter 16

It is worth noting that KIC9655315 had the most consistent period, with minimal aliasing within in quarters. It also had the most definitive power spectrum, with *theta* values routinely above 100.

In contrast, KIC9716650 was plagued by low *theta* values and heavy aliasing, with multiple lightcurves showing no discernable period. The reason for these variations may be physically interesting, the result of some occultation of the star, or some disruption of the magnetic dynamo, but that is beyond the scope of this study. For the purpose of

activity-cycle studies, this variation is disruptive, and KIC9716650 seems like a poor choice as a result.

KIC9715987 Does show definitive periods, with fewer instances of apparent aliasing within the lightcurves, compared to KIC9716650. It is still characterized by low *theta* values within the periodogram, especially compared to KIC9655315, and its variation in flux is much lower than KIC9655315. This would make it more difficult to detect these variations with ground-based technology.

Conclusions

After examining each of these datasets, it seems that the 2007 dataset is too noisy to be useful in this context. Although there is plentiful data, the nightly variation is too high to see anything meaningful in these stars. Therefore, this data should likely be removed from further study.

The 2013 and 2014 is much less definitive. There does not seem to be enough data to definitively determine if stellar variation is present, but this could also be related to the color issue discussed above. To know whether the color issue precludes the use of this data, additional images taken alongside reference images would be required. Future studies could also attempt to select target stars that more closely matched the reference stars to bypass the color issue completely.

The Kepler data would appear to be the most definitive with these stars, indicating that KIC9655315 is the most viable candidate. The periodicity of this star is the most consistent of the stars, and because of its large *theta* values, it was much more resistant to aliasing than the others. KIC9715987 showed some consistency in periods, with only a couple lightcurves exhibiting an alias period as the dominant one, but low *theta* values

made it more difficult to determine the true period. Were Kepler observations to continue, both KIC9715987 and KIC9655315 could be potential activity-cycle candidates given the clarity of their lightcurves, but because of the end of the original Kepler missions, future observations will be from ground-based observatories. This precludes KIC9715987 from study dues to its relatively small amplitude of variation. As a result, KIC9655315 seems to be the most viable candidate for continued ground-based study, with the reservations related to color and sample size enumerated above.

Additional Lightcurves
KIC9655315

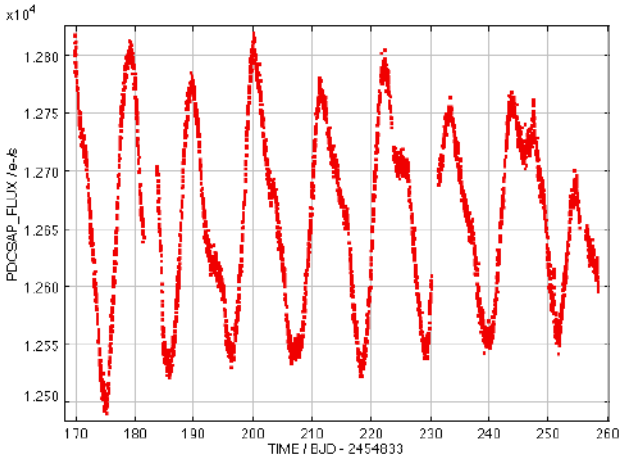

Graph 7: KIC9655315 Lightcurve for Quarter 2

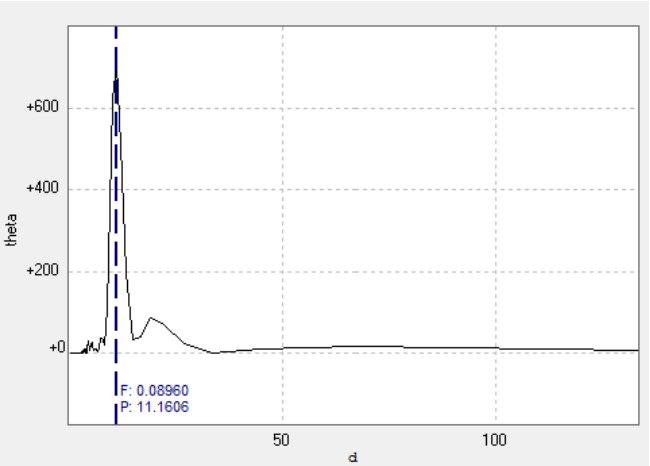

Figure 26: KIC9655315 Periodogram for Quarter 2

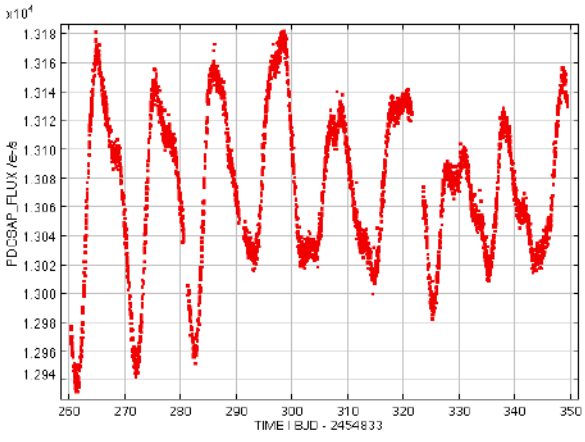

Graph 8: KIC9655315 for Quarter 3

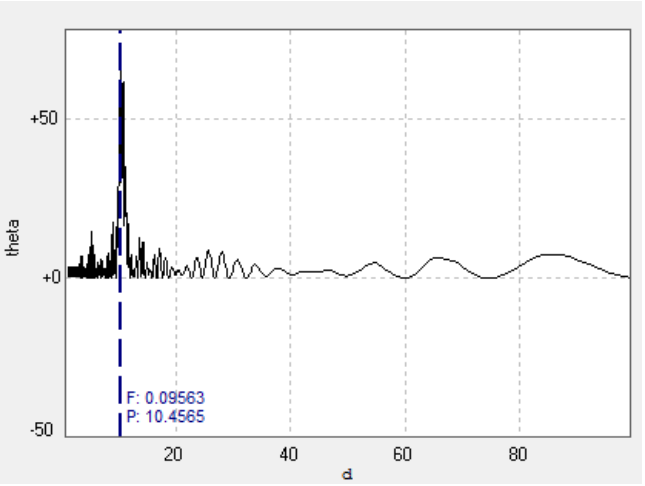

Figure 27: KIC9655315 Periodogram for Quarter 3

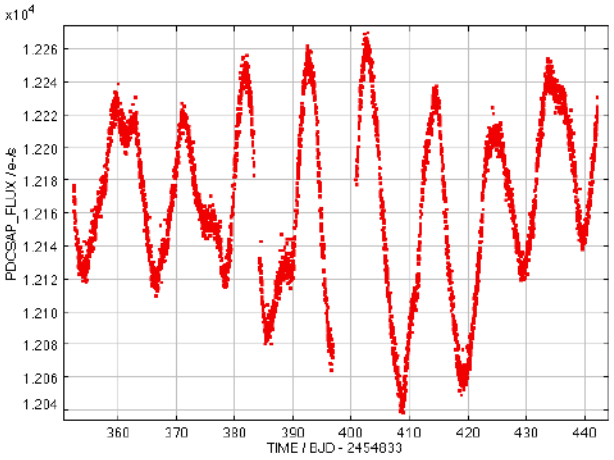

Graph 9: KIC9655315 Lightcurve for Quarter 4

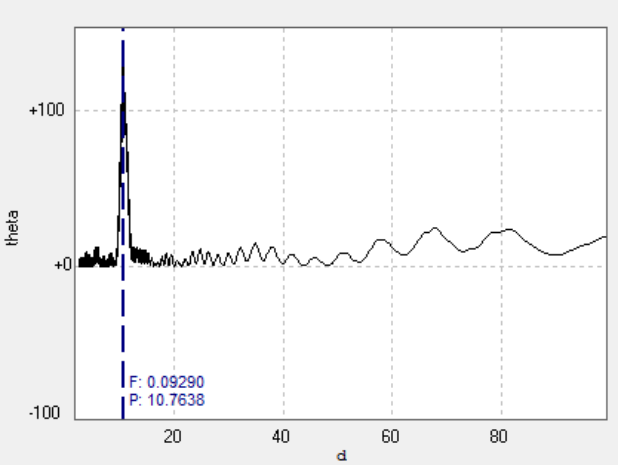

Figure 28: KIC9655315 Periodogram for Quarter 4

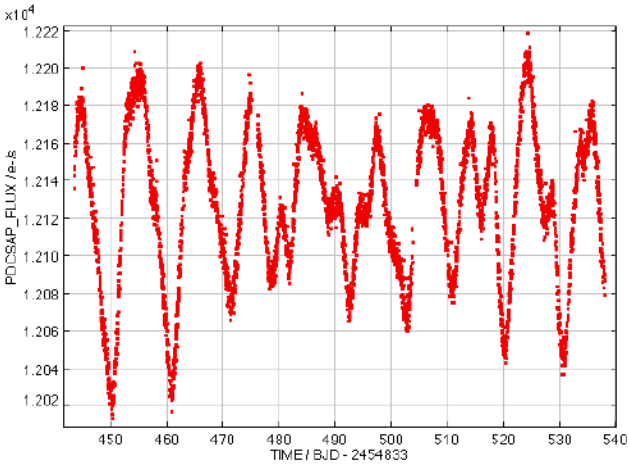

Graph 10: KIC9655315 Quarter 5

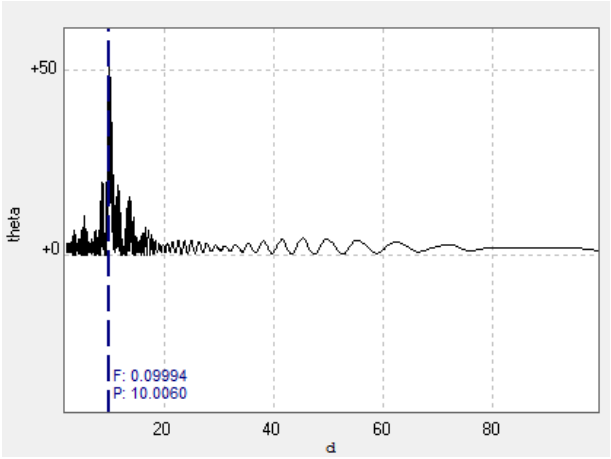

Figure 29: KIC9655315 for Quarter 5

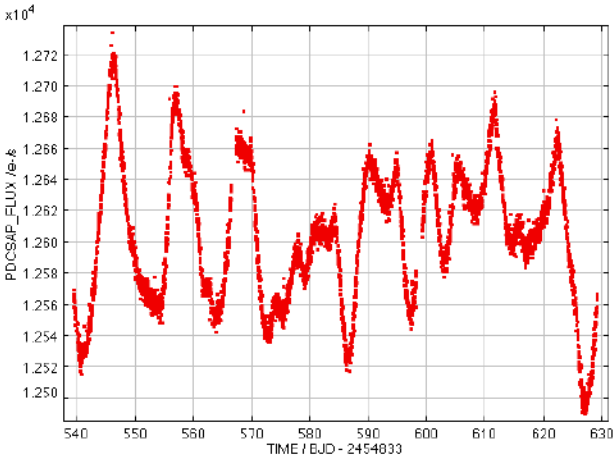

Graph 11: KIC9655315 Quarter 6

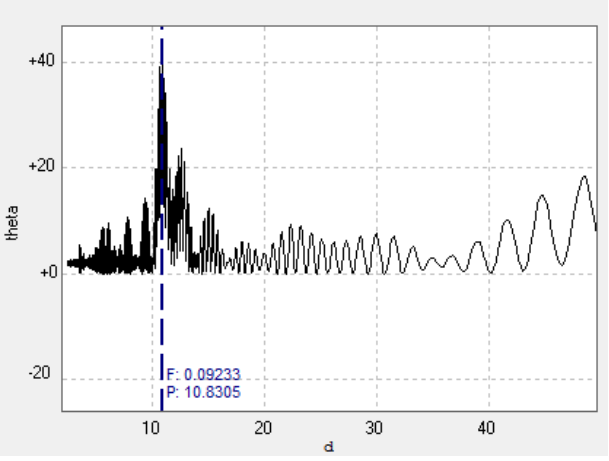

Figure 30: KIC9655315 for Quarter 6

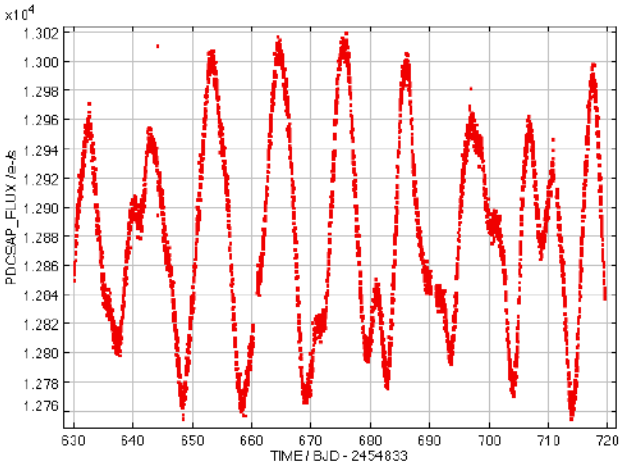

Graph 10: KIC9655315 Quarter 7

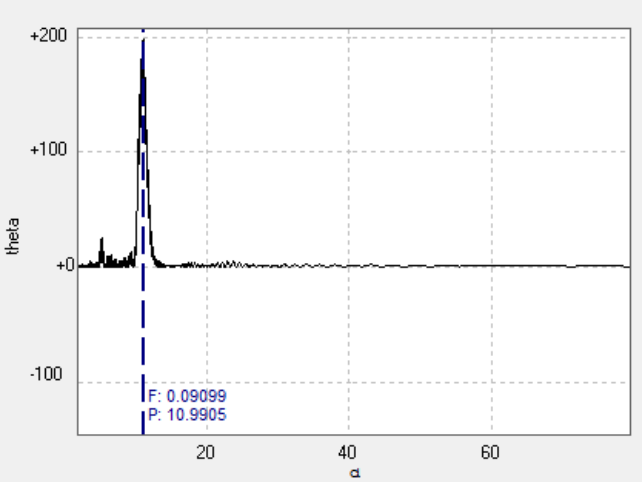

Figure 31: KIC9655315 Quarter 7

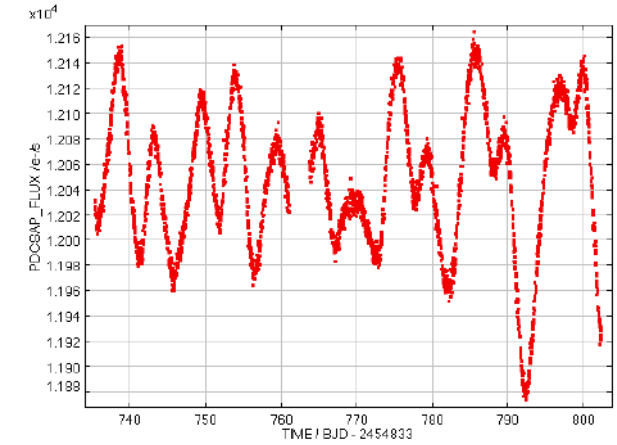

Graph 11: KIC9655315 Quarter 8

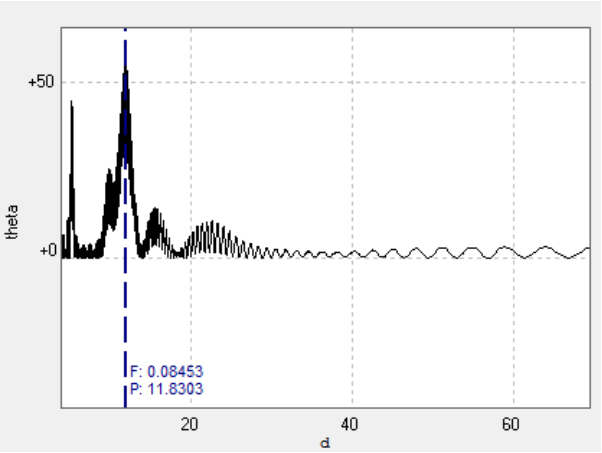

Figure 32: KIC9655315 Quarter 8

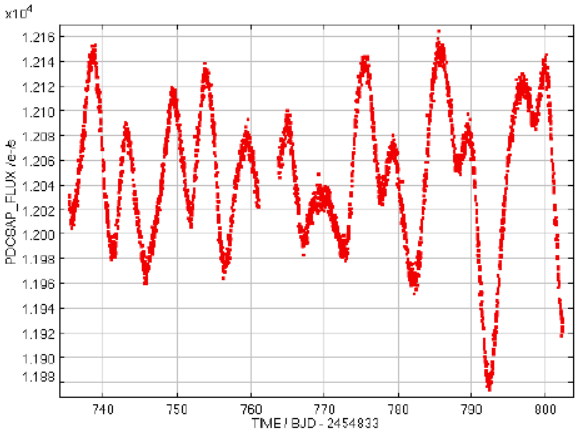

Graph 12: KIC9655315 for Quarter 9

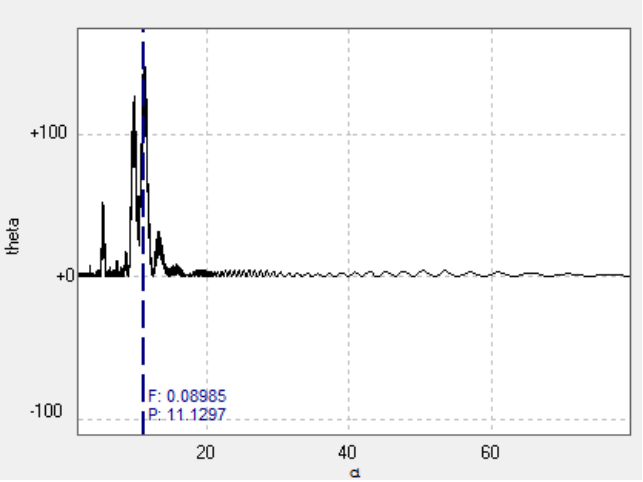

Figure 33: KIC9655315 for Quarter 9

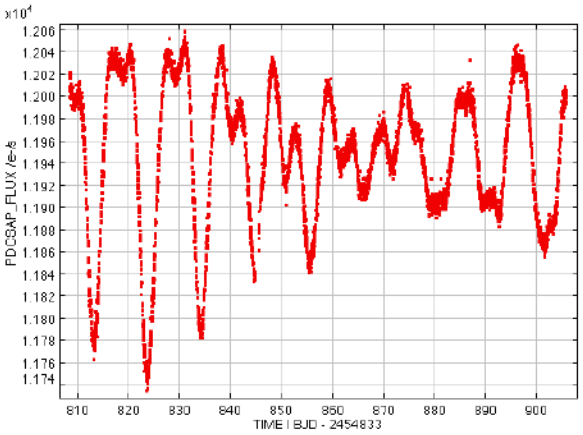

Graph 13: KIC9655315 Quarter 10

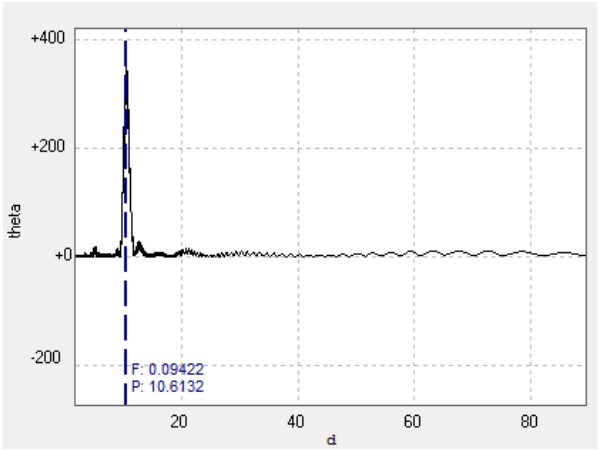

Figure 34: KIC9655315 Quarter 10

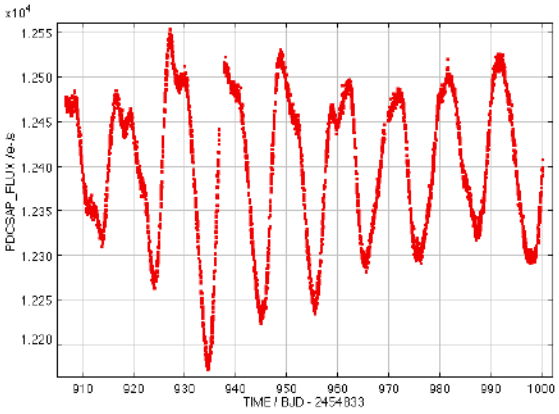

Graph 14: KIC9655315 Quarter 11

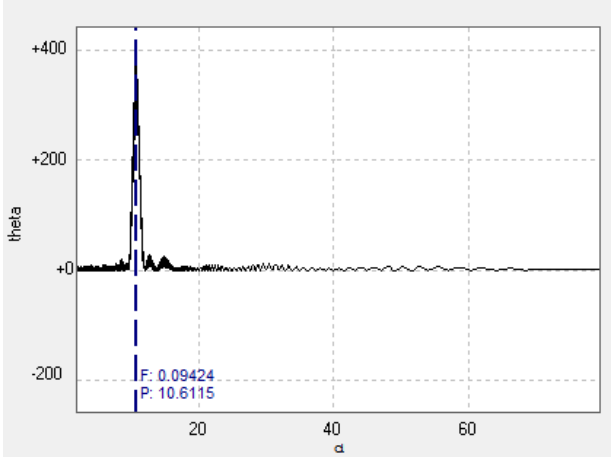

Figure 35: KIC9655315 Quarter 11

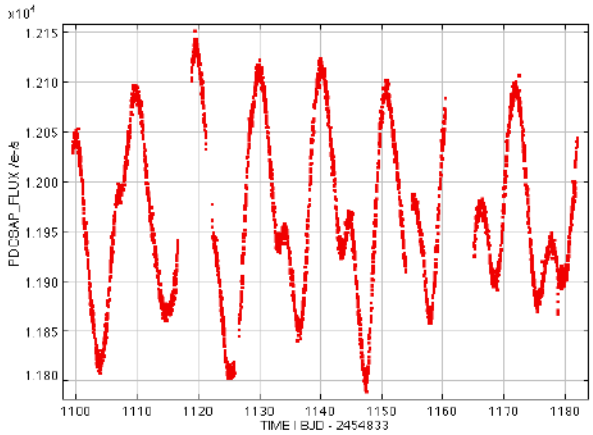

Graph 15: KIC9655315 Quarter 12

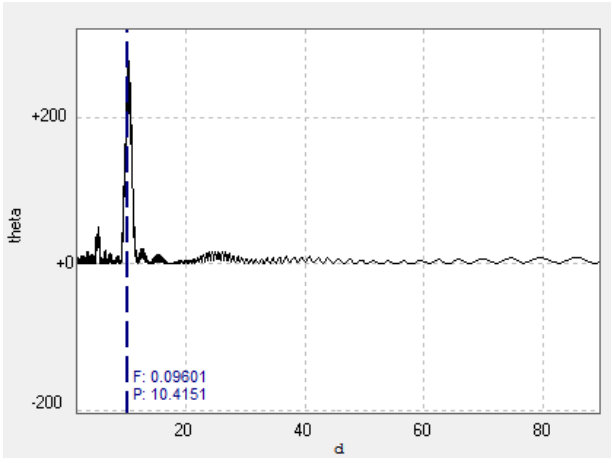

Figure 36: KIC9655315 Quarter 12

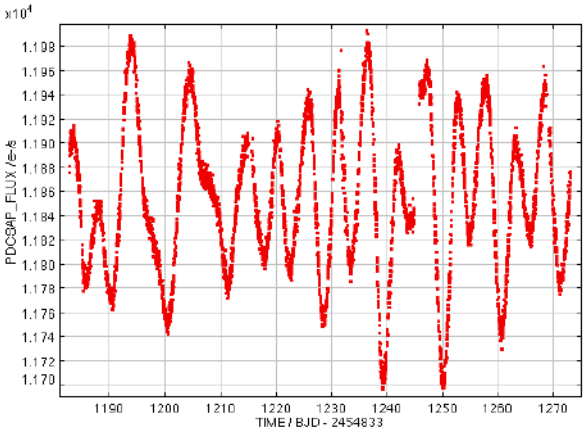

Graph 16: KIC9655315 Quarter 13

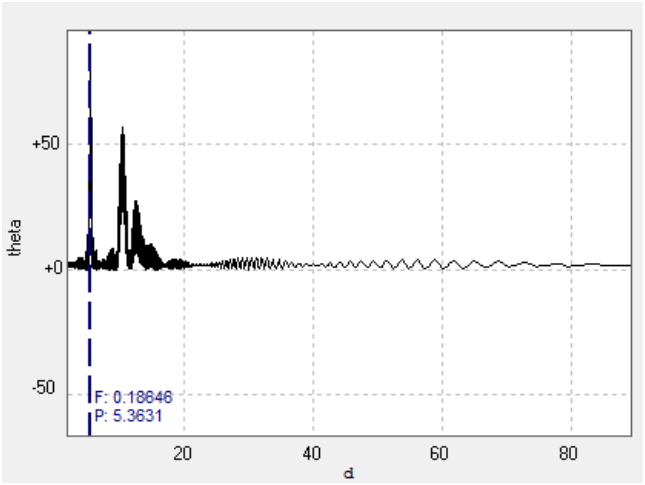

Figure 37: KIC9655315 Quarter 13

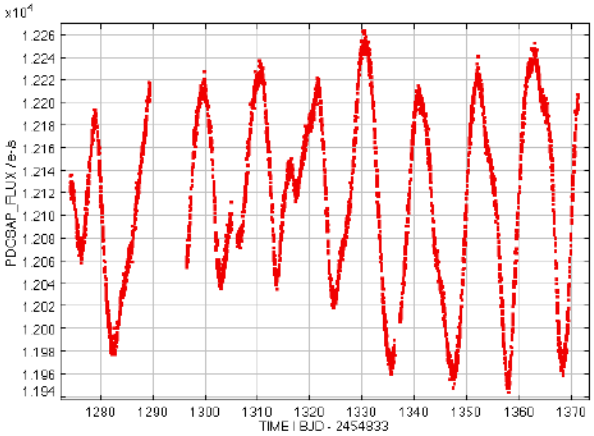

Graph 19: KIC9655315 Quarter 14

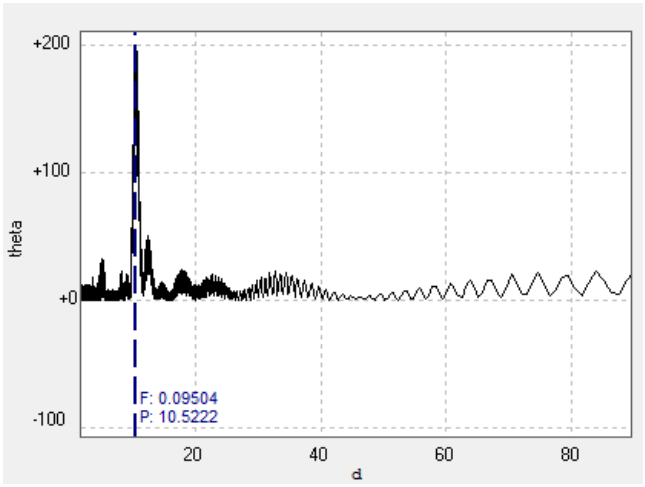

Figure 38: KIC9655315 Quarter 14

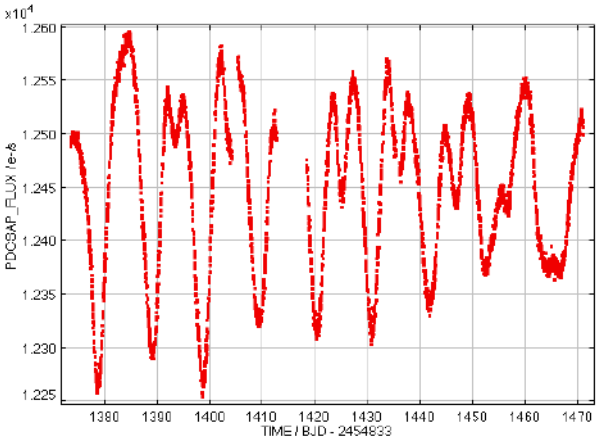

Graph 20: KIC9655315 Quarter 15

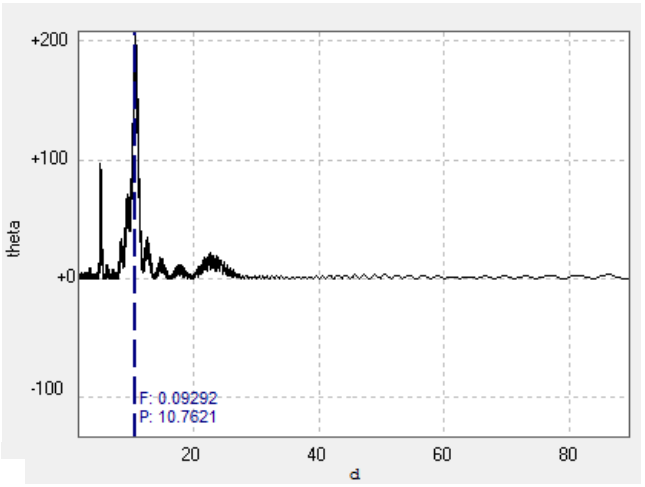

Figure 39: KIC9655315 Quarter 15

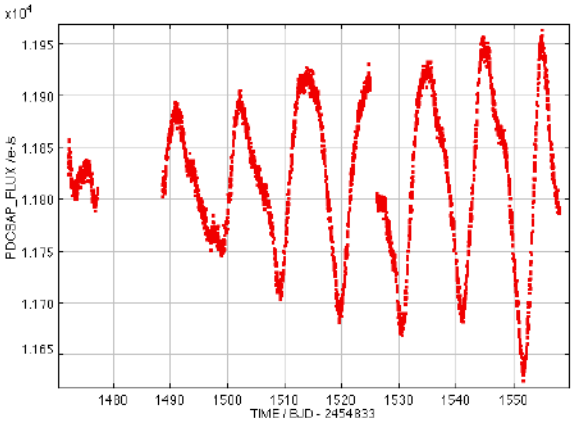

Graph 17: KIC9655315 Quarter 16

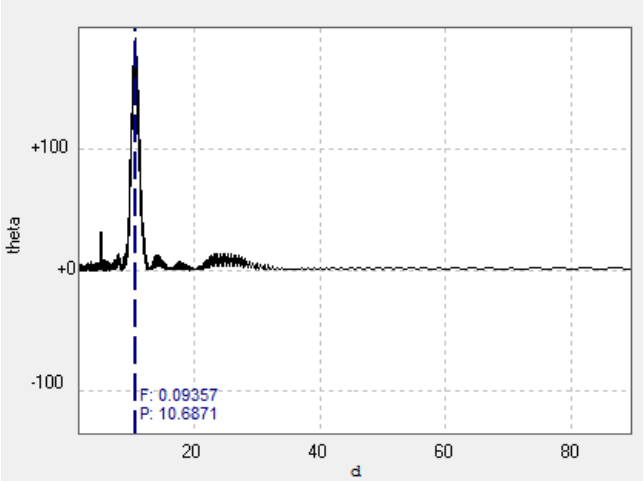

Figure 40: KIC9655315 Quarter 16

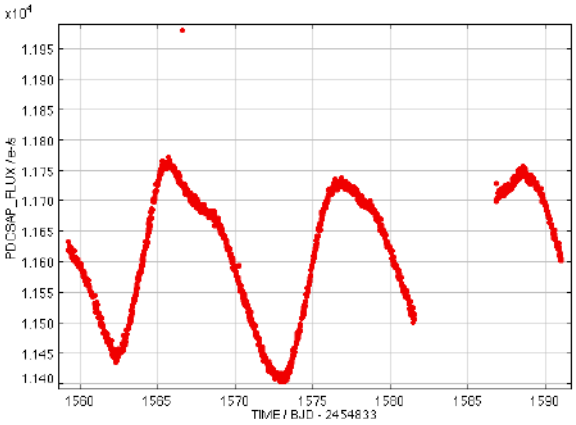

Graph 18: KIC9655315 Quarter 17

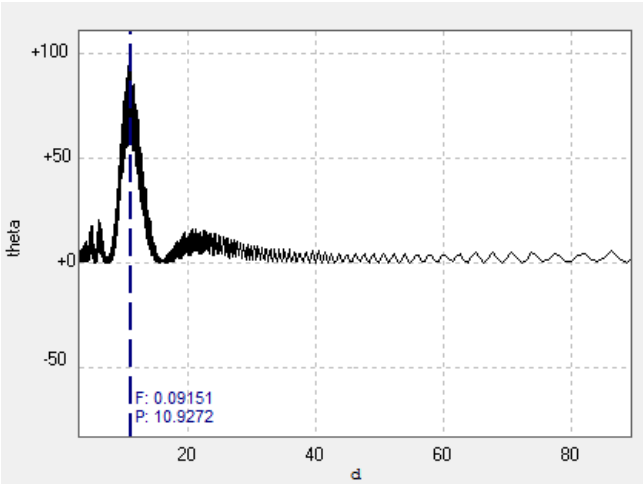

Figure 41: KIC9655315 Quarter 17

KIC9715987

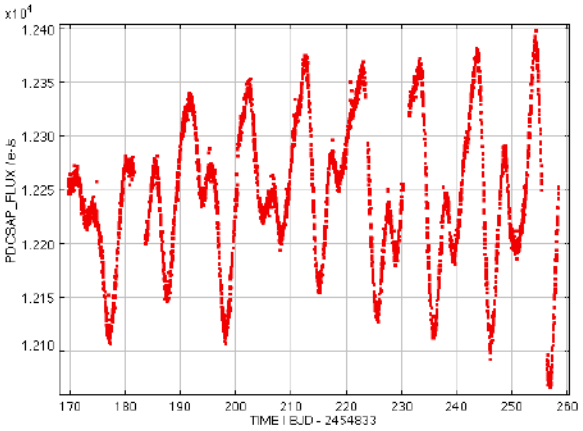

Graph 19: KIC9715987 Quarter 2

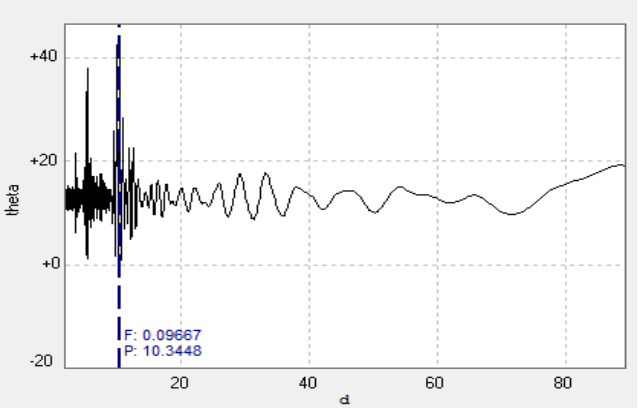

Figure 42: KIC9715987 Quarter 2

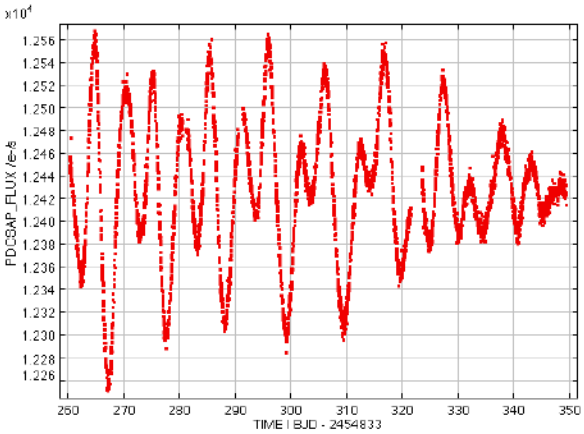

Graph 20: KIC9715987 Quarter 3

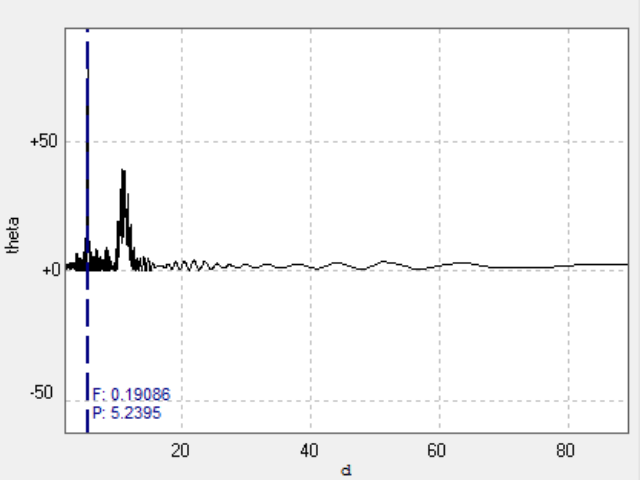

Figure 43: KIC9715987 Quarter 3

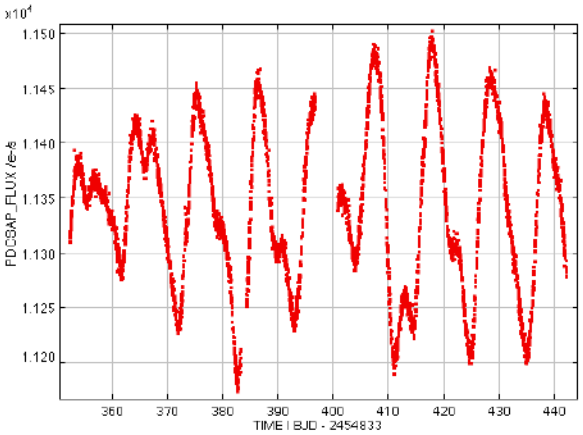

Graph 25: KIC9715987 Quarter 4

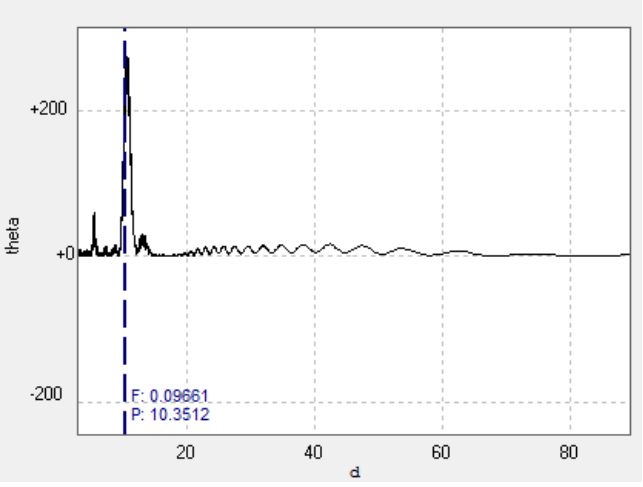

Figure 44: KIC9715987 Quarter 4

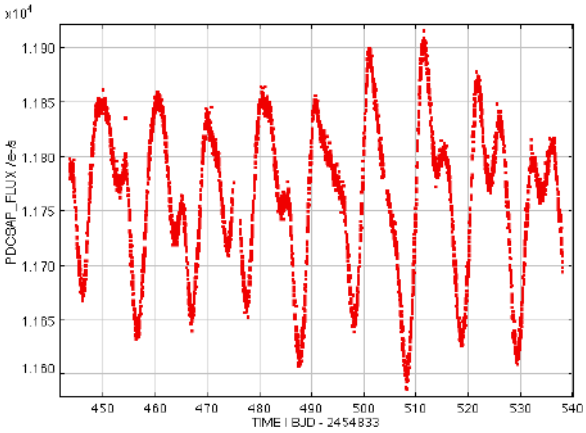

Graph 21: KIC9715987 Quarter 5

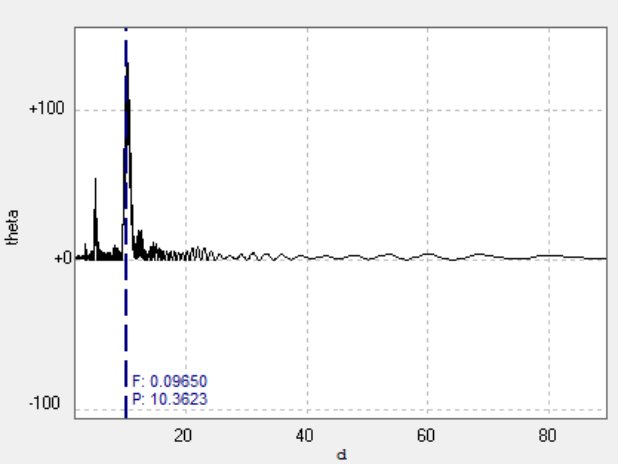

Figure 45: KIC9715987 Quarter 5

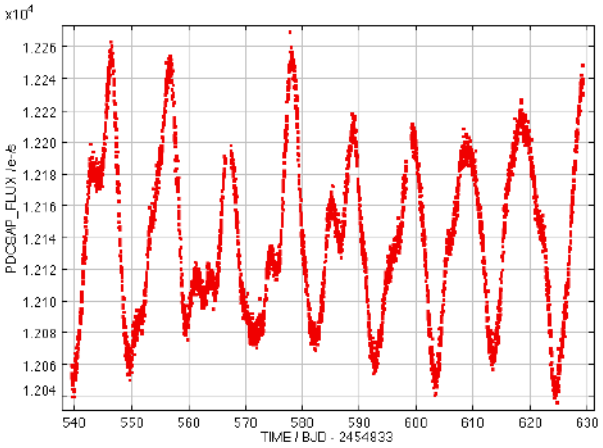

Graph 22: KIC9715987 Quarter 6

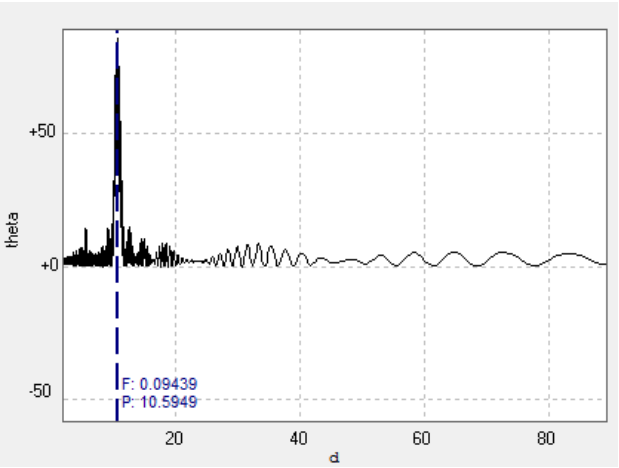

Figure 46: KIC9715987 Quarter 6

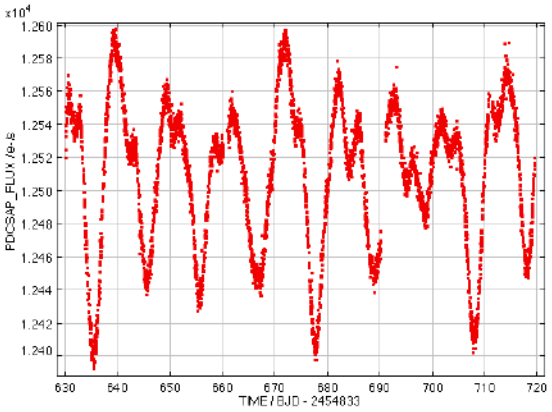

Graph 28: KIC9715987 Quarter 7

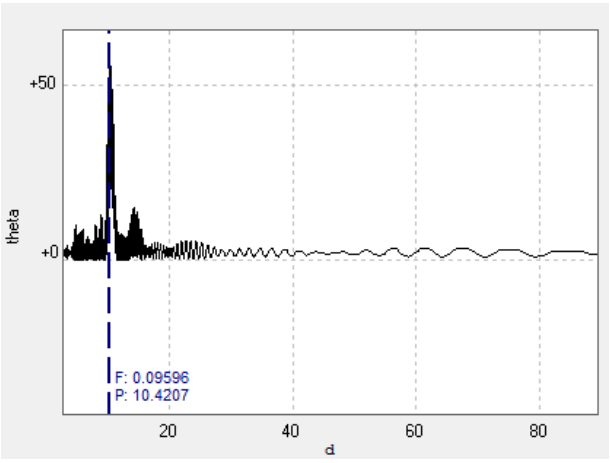

Figure 47: KIC9715987 Quarter 7

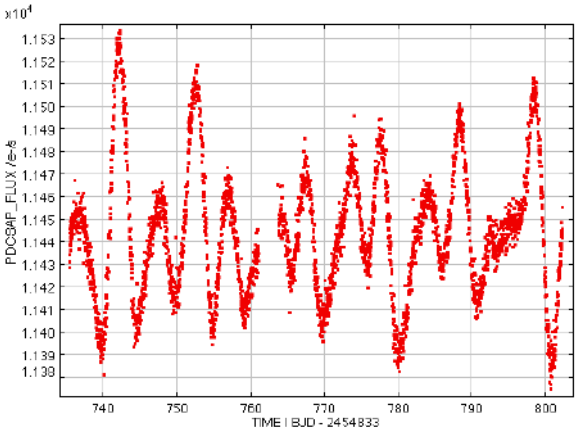

Graph 23: KIC9715987 Quarter 8

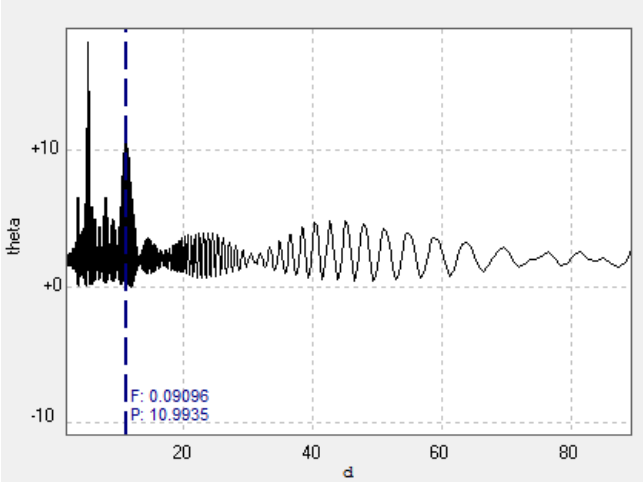

Figure 48: KIC9715987 Quarter 8

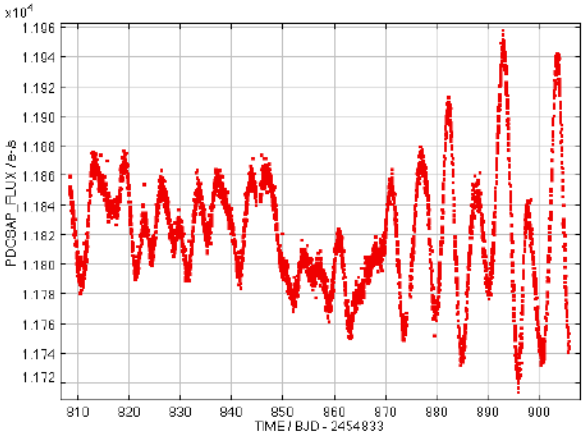

Graph 24: KIC9715987 Quarter 9

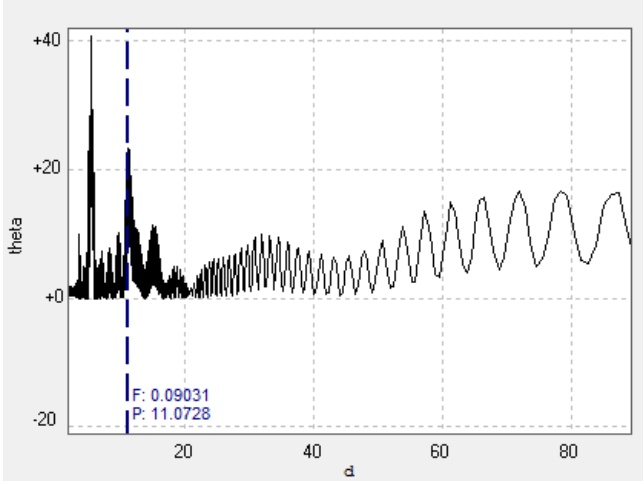

Figure 49: KIC9715987 Quarter 9

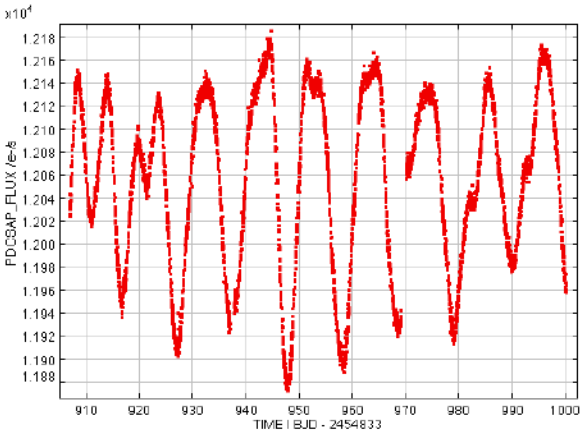

Graph 31:KIC9715987 Quarter 10

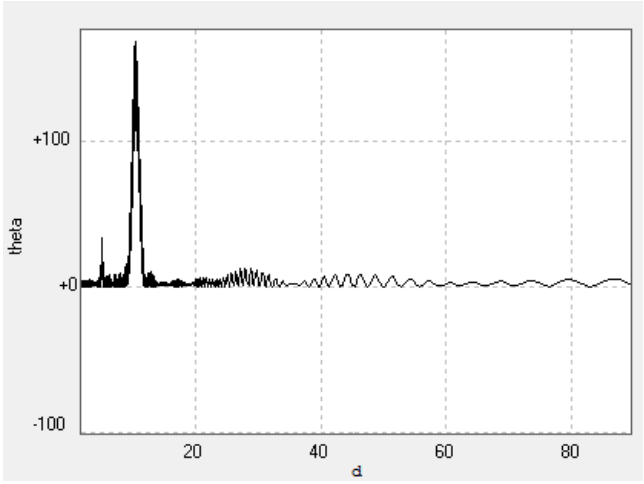

Figure 50: KIC9715987 Quarter 10

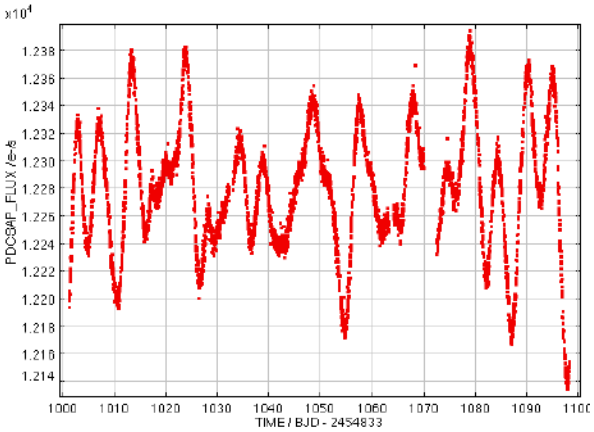

Graph 25: KIC9715987 Quarter 11

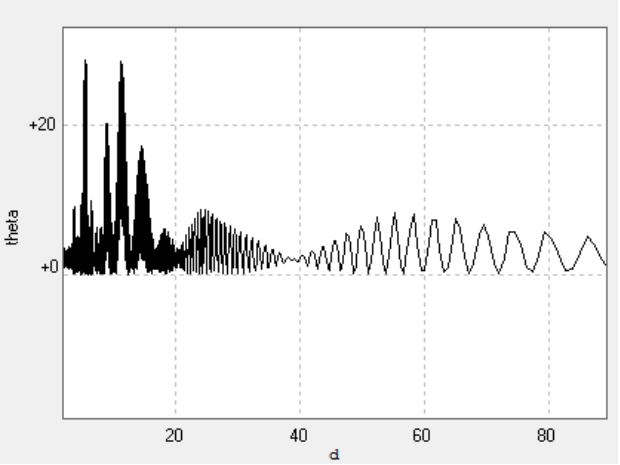

Figure 51: KIC9715987 Quarter 11

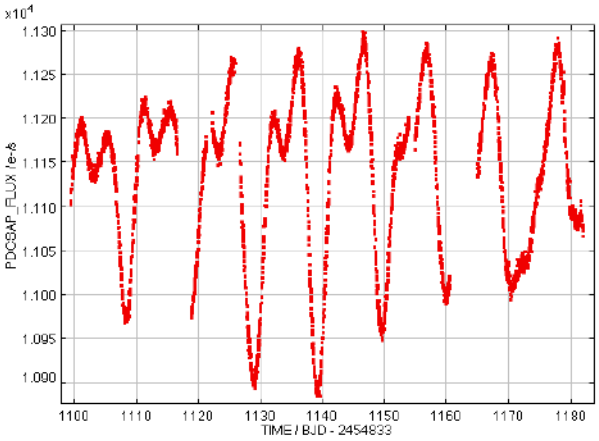

Graph 26: KIC9715987 Quarter 12

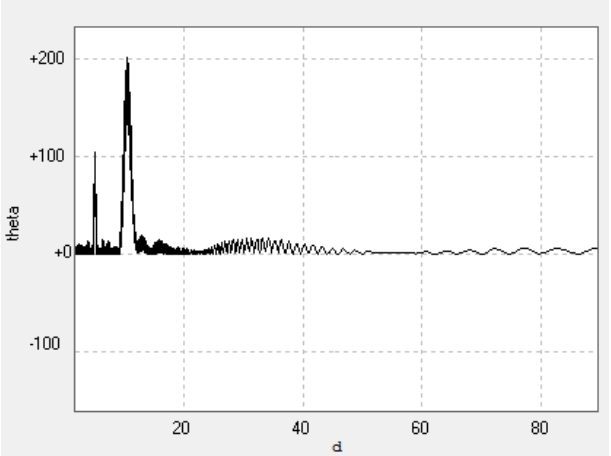

Figure 52: KIC9715987 Quarter 12

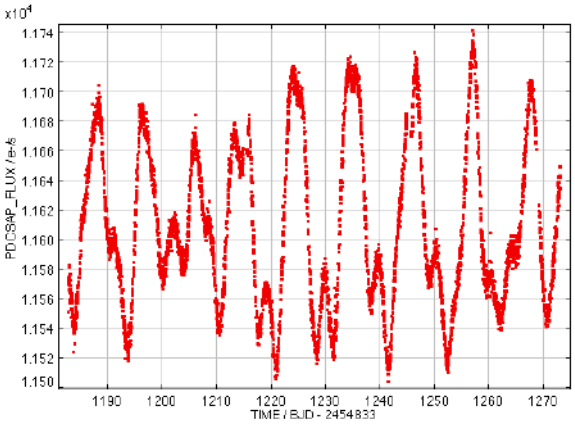

Graph 34: KIC9715987 Quarter 13

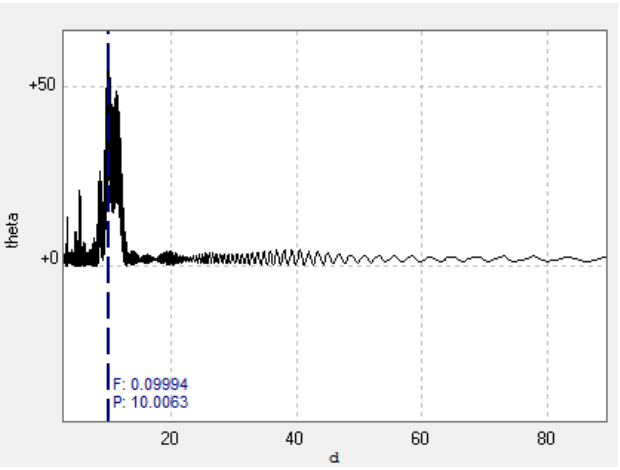

Figure 53: KIC9715987 Quarter 13

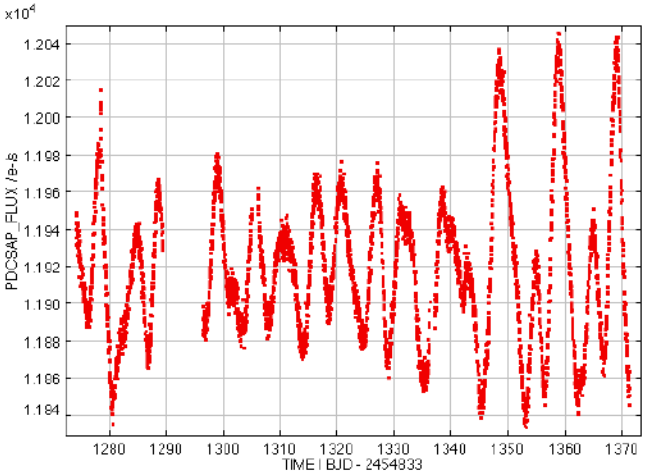

Graph 27: KIC9715987 Quarter 14

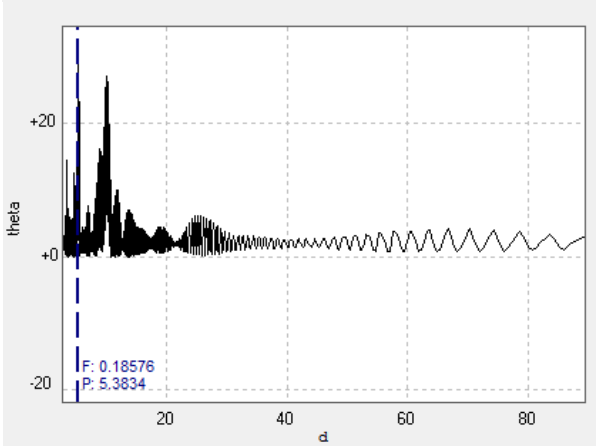

Figure 54: KIC9715987 Quarter 14

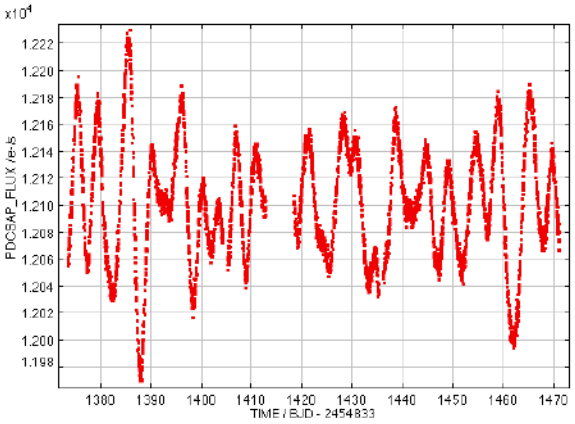

Graph 28: KIC9715987 Quarter 15

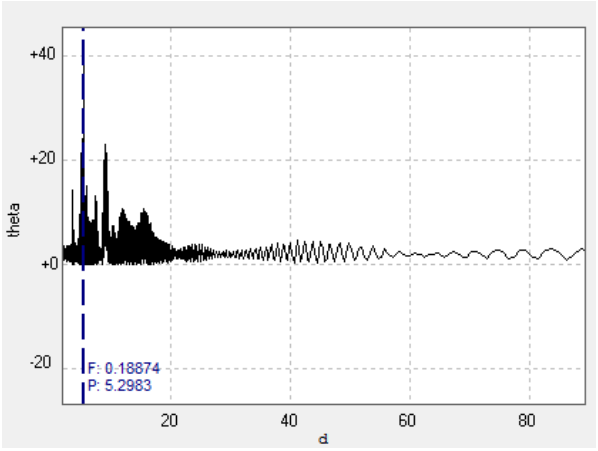

Figure 55: KIC9715987 Quarter 15

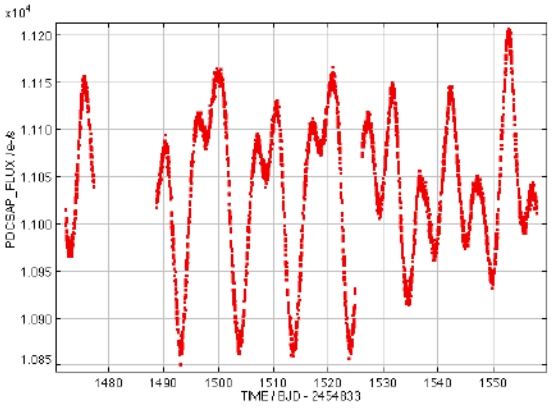

Graph 37: KIC9715987 Quarter 16

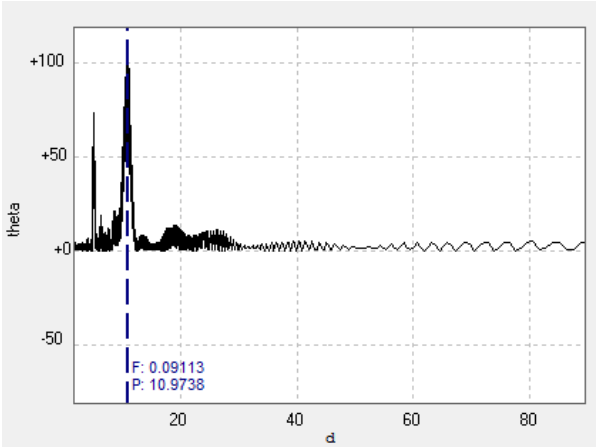

Figure 56: KIC9715987 Quarter 16

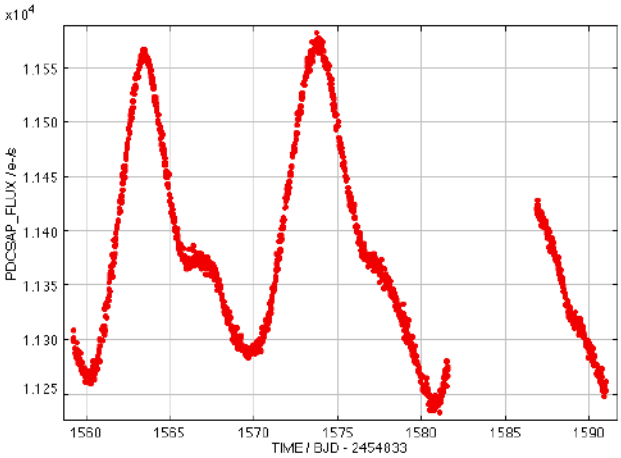

Graph 29: KIC9715987 Quarter 17

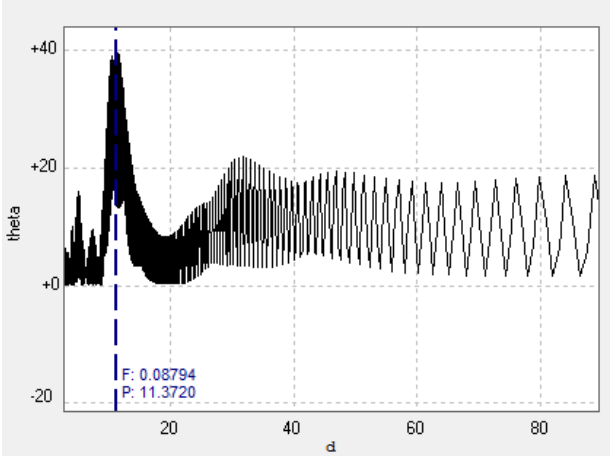

Figure 57: KIC9715987 Quarter 17

KIC9716650

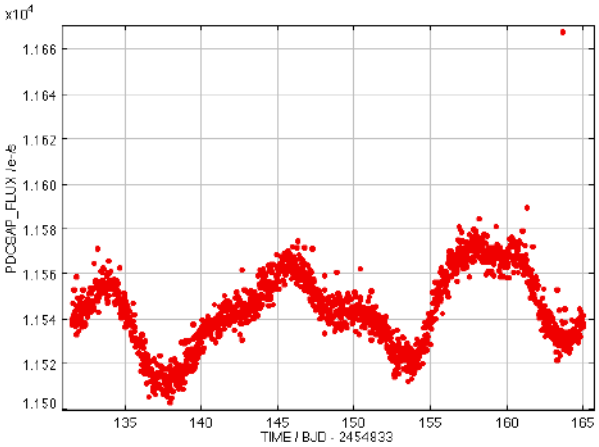

Graph 30: KIC9716650 Quarter 1

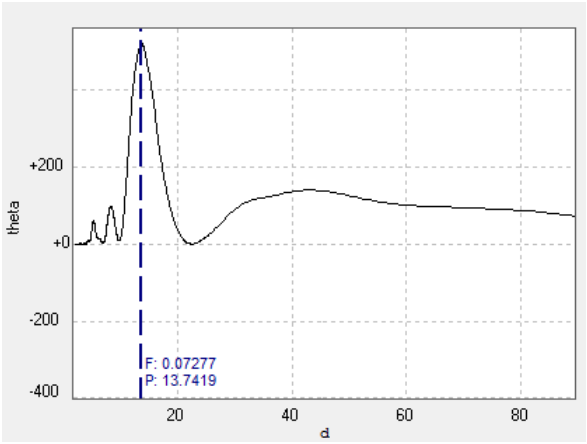

Figure 58: KIC9716650 Quarter 1

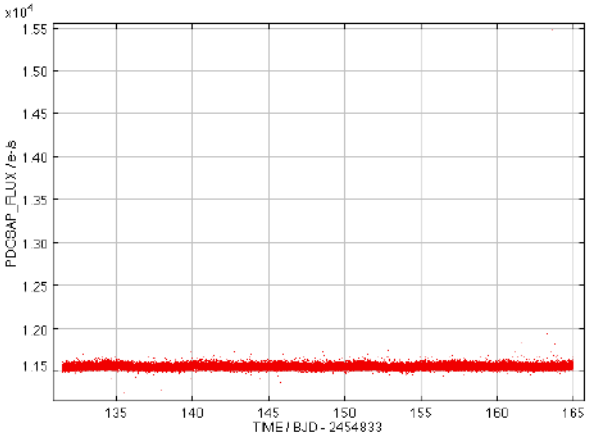

Graph 31: KIC9716650 Quarter 2

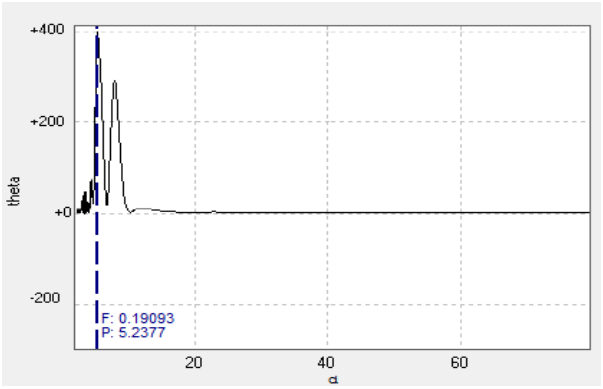

Figure 59: KIC9716650 Quarter 2

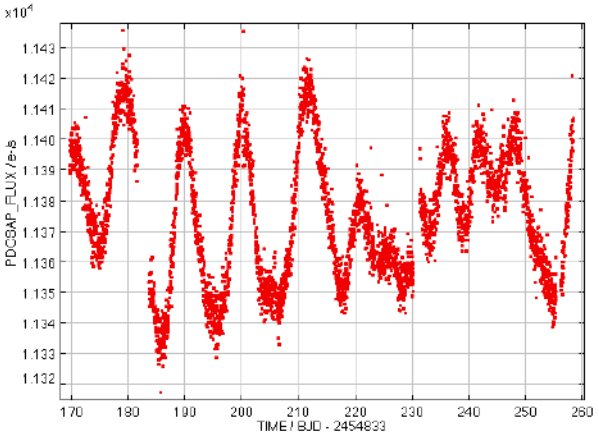

Graph 41: KIC9716650 Quarter 3

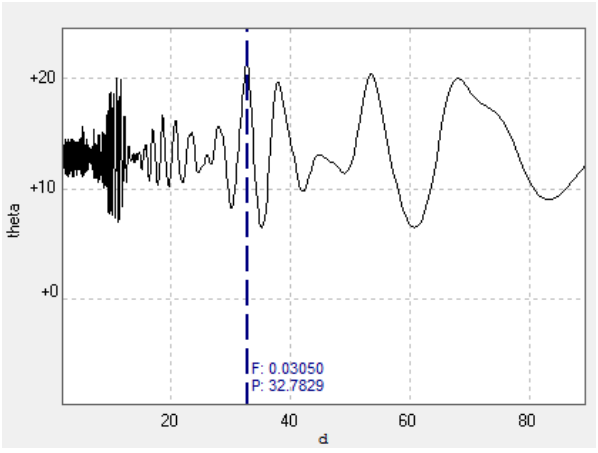

Figure 60: KIC9716650 Quarter 3

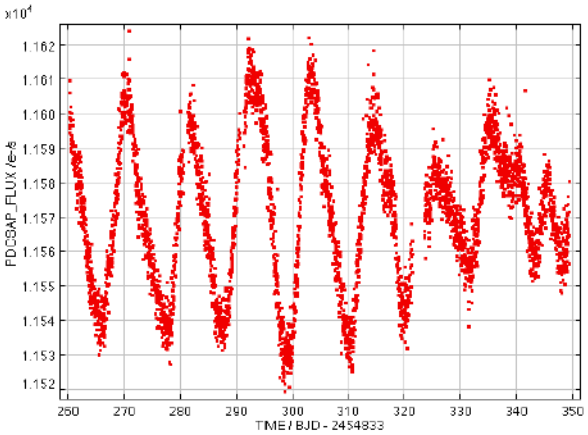

Graph 32: KIC9716650 Quarter 4

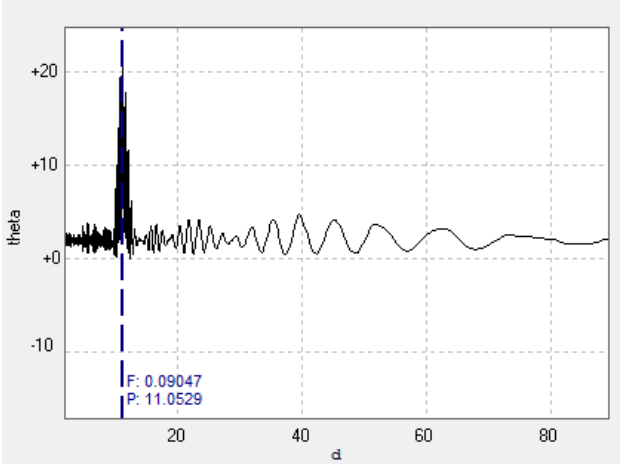

Figure 61: KIC916550 Quarter 4

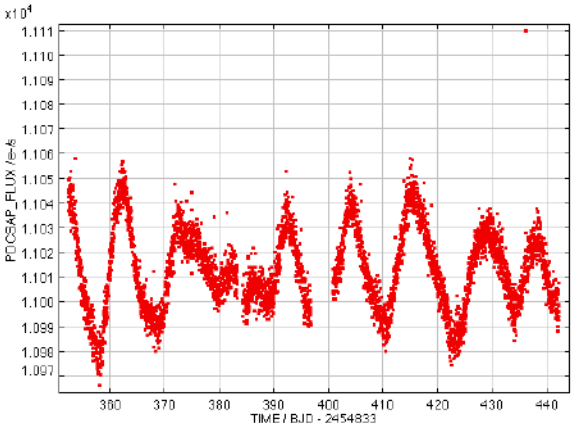

Graph 33: KIC9715987 Quarter 5

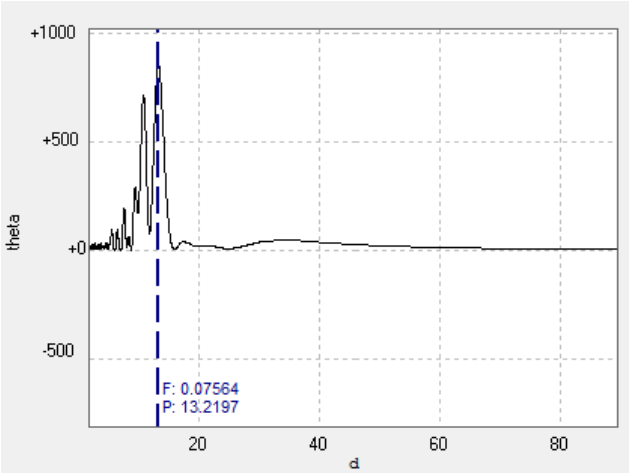

Figure 62: KIC9716650 Quarter 5

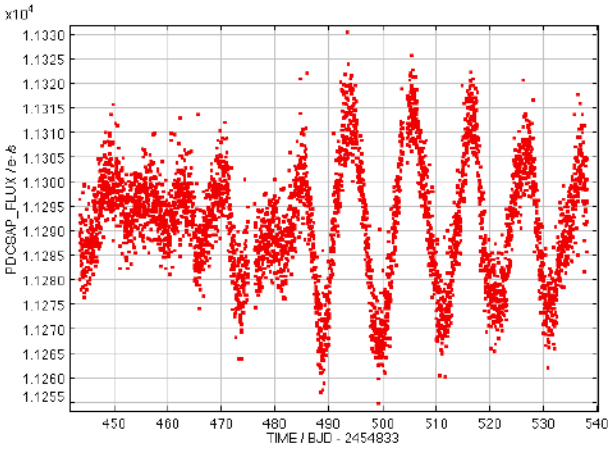

Graph 44: KIC9715987 Quarter 6

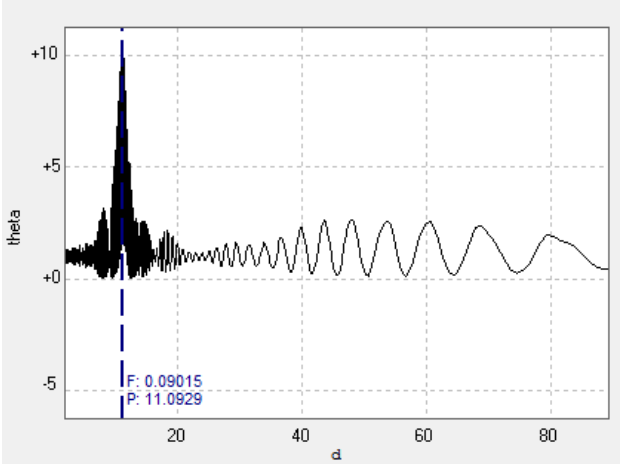

FIgure 63: KIC9716650 Quarter 6

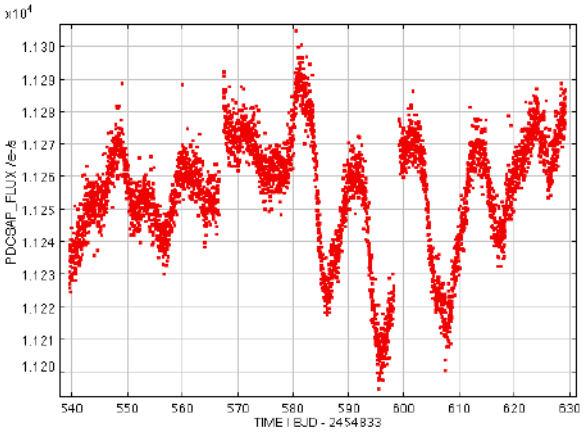

Graph 45:KIC9716650 Quarter 7

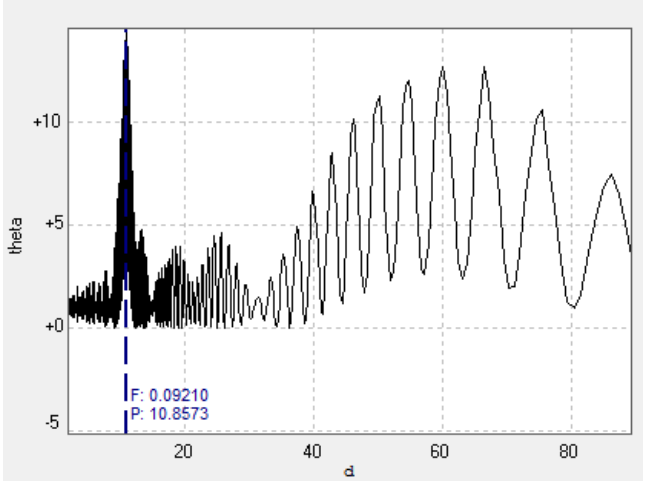

Figure 64:KIC9716650 Quarter 7

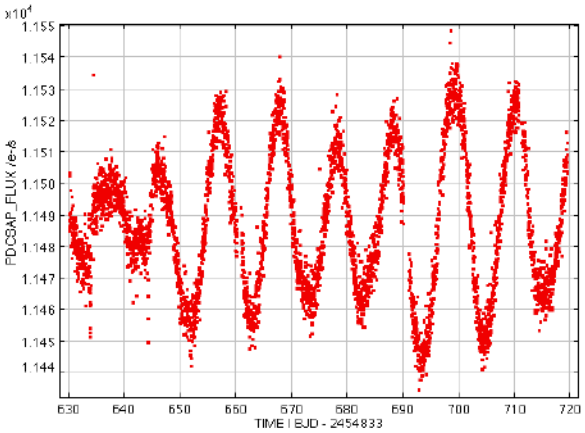

Graph 46: KIC9716650 Quarter 8

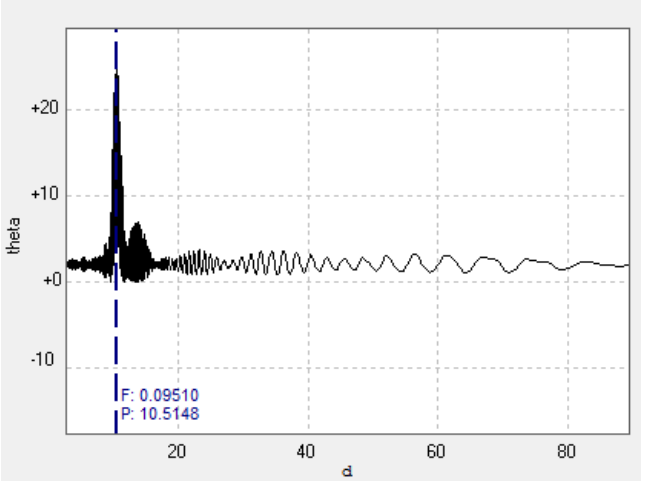

Figure 65: KIC9716650 Quarter 8

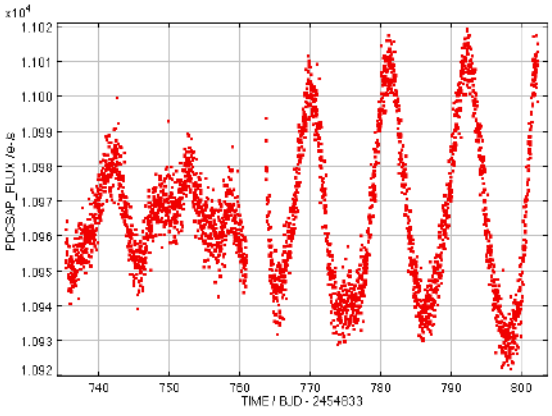

Graph 34: KIC9716650 Quarter 9

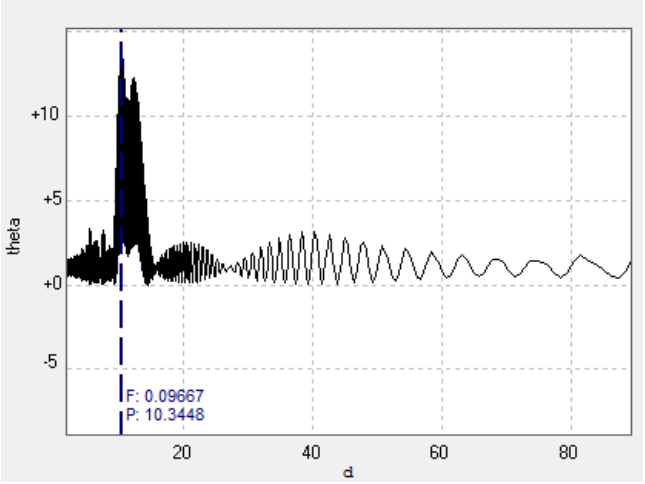

Figure 66: KIC9716650 Quarter 9

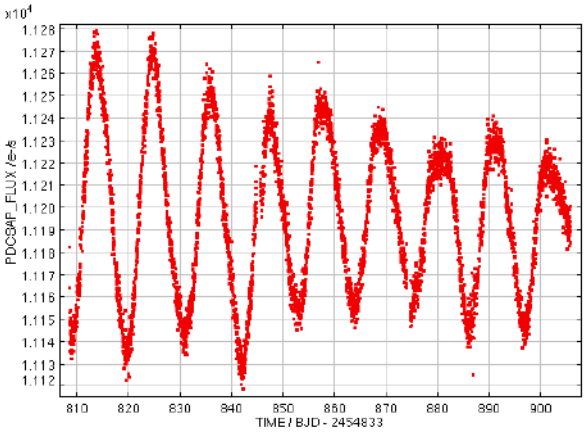

Graph 48: KIC9716650 Quarter 10

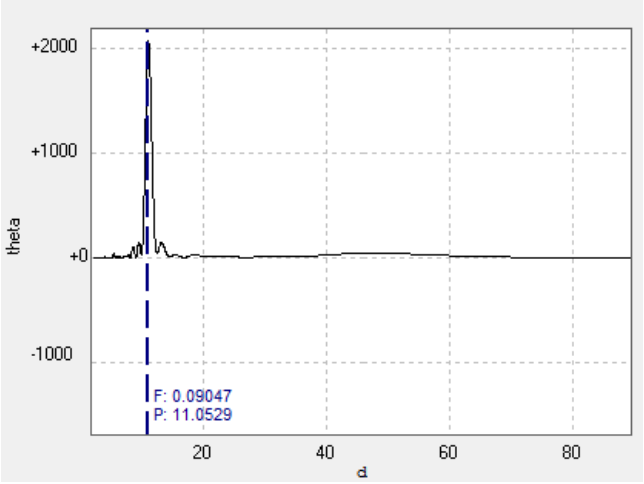

Figure 67: KIC9716650 Quarter 10

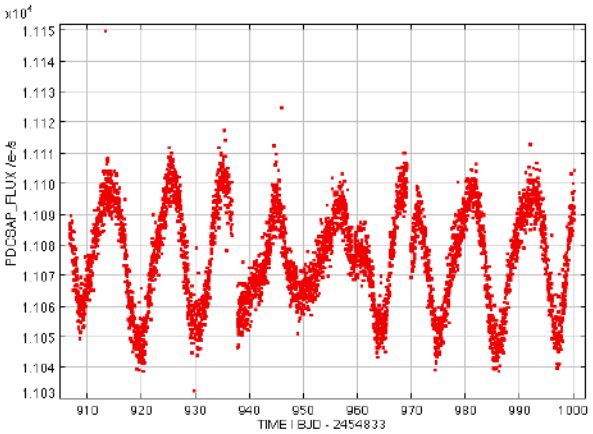

Graph 49: KIC9716650 Quarter 11

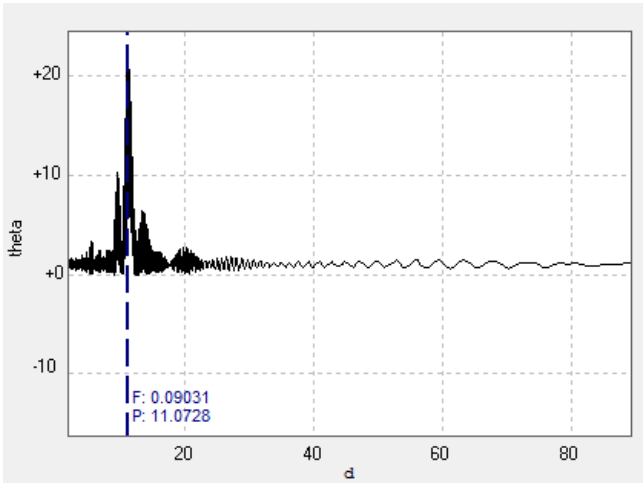

Graph 68: KIC9716650 Quarter 11

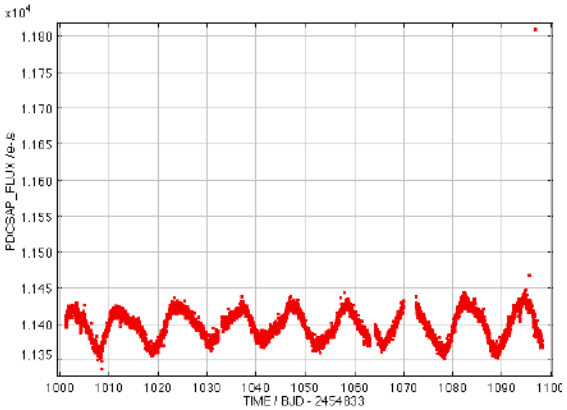

Graph 35: KIC9716650 Quarter 12

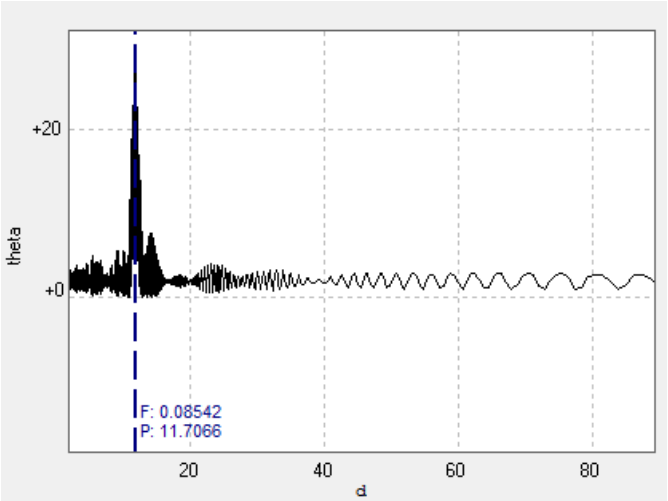

Figure 69: KIC9716650 Quarter 12

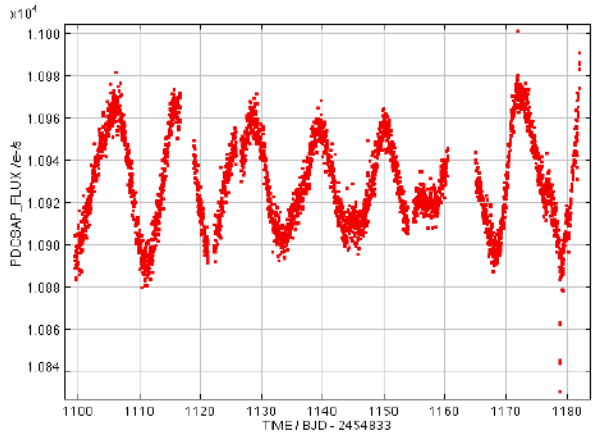

Graph 51: KIC9716650 Quarter 13

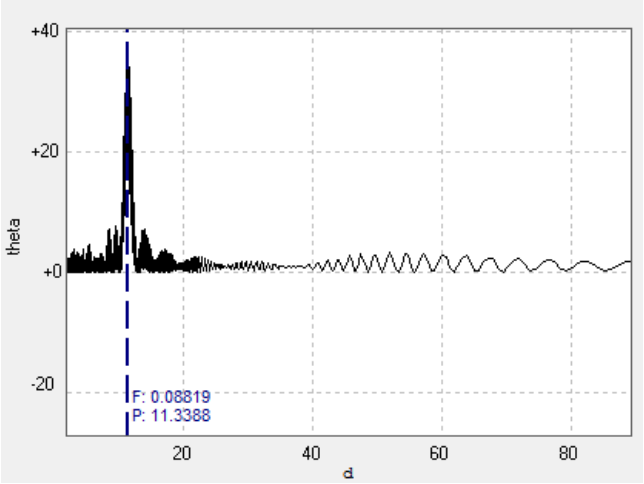

Figure 70: KIC9716650 Quarter 13

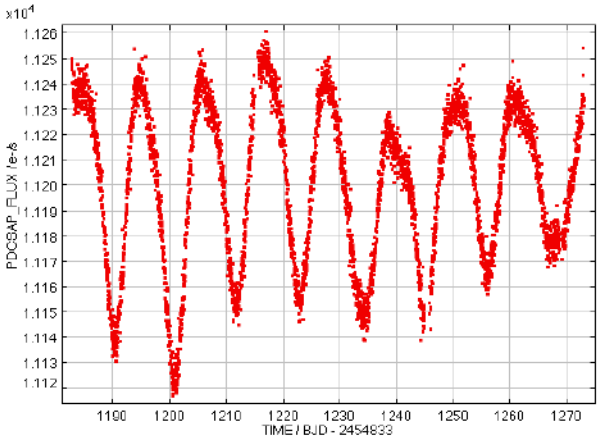

Graph 52: KIC9716550 Quarter 14

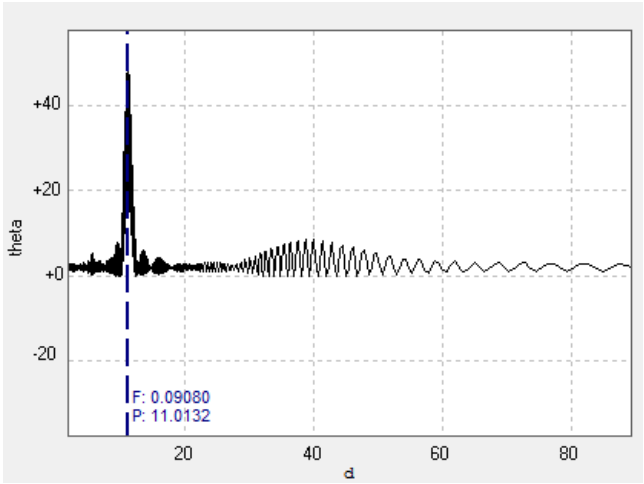

Figure 71: KIC9716650 Quarter 14

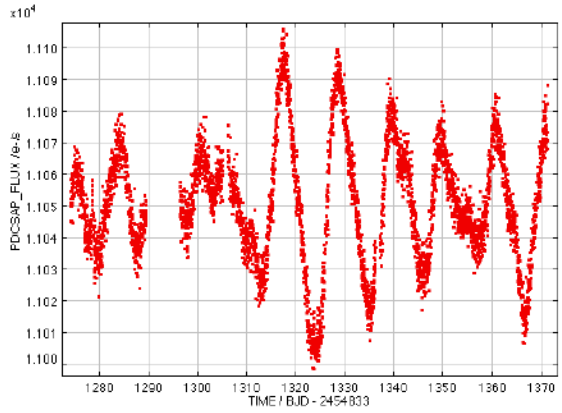

Graph 36: KIC9716650 Quarter 15

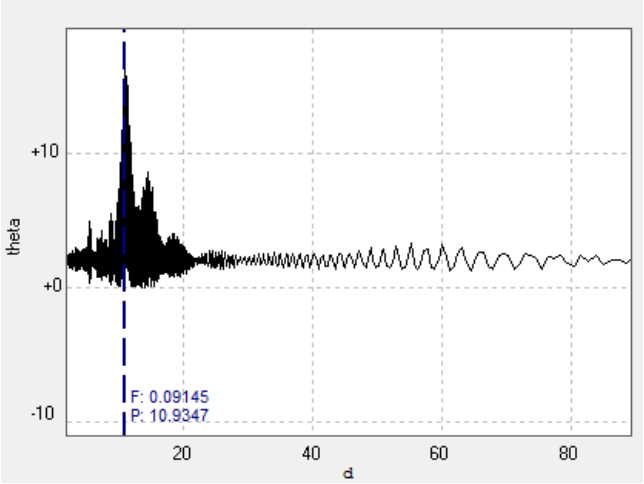

Figure 72: KIC9716650 Quarter 15

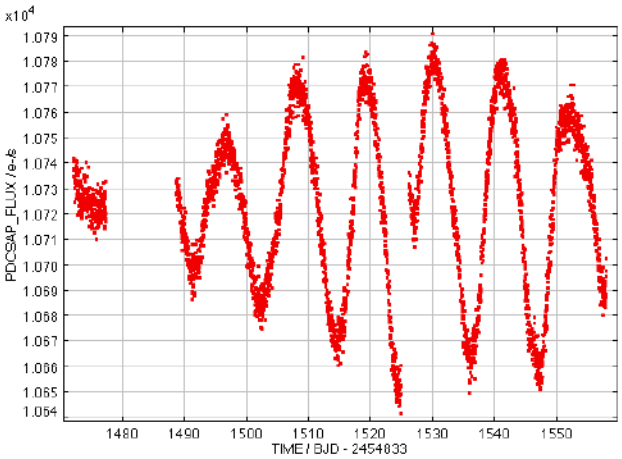

Graph 55: KIC9716650 Quarter 17

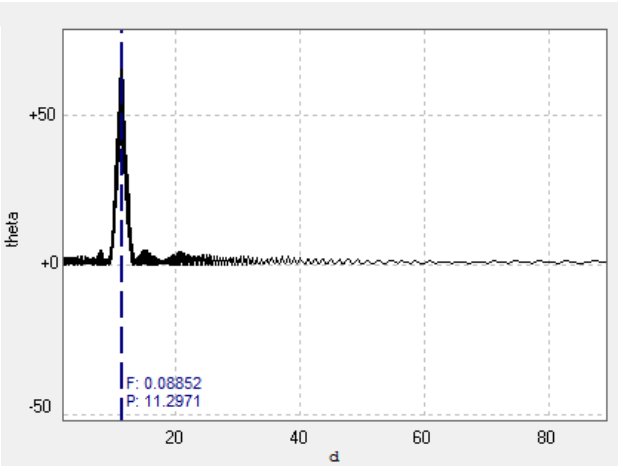

Figure 73: KIC9716650 Quarter 17

References

[1] Tobias, Steven, and Nigel Weiss. "CHAPTER 6 STELLAR DYNAMOS." *Grenoble Sciences*. Grenoble. <https://grenoble-sciences.ujf-grenoble.fr/sites/default/files/pdf/ouvrages/extraits/17332021.pdf>.

[2] Vecchio, A., M. Laurenza, D. Meduri, V. Carbone, and M. Storini. "The Dynamics Of The Solar Magnetic Field: Polarity Reversals, Butterfly Diagram, And Quasi-Biennial Oscillations." *The Astrophysical Journal* 749.1 (2012): 27.

[3] Milingo, J. B., S. H. Saar, L. A. Marschall, and J. R. Stauffer. "Rotational Modulation, Shear, and Cyclic Activity in HII 1883." *Proceedings of the International Astronomical Union* 6.S273 (2010): 74-77.

[4] Seeds, Michael A., and Dana E. Backman. *Foundations of Astronomy*. Boston, MA: Brooks/Cole, Cengage Learning, 2013.

[5] Cousins, Adam. "Index of /faculties/science/astronomy/jwest/projects/adam/Research Assignment on Stellar Corpses/graphics." *Index of /faculties/science/astronomy/jwest/projects/adam/Research Assignment on Stellar Corpses/graphics*. University of Manitoba, n.d. Web. <http://umanitoba.ca/faculties/science/astronomy/jwest/projects/adam/Research%20Assignment%20on%20Stellar%20Corpses/graphics/>

[6] Pols, O. R. "Chapter 4: Energy Transport in Stellar Interiors." *Stellar Structure and Evolution*. N.p.: n.p., n.d. 43-64.

[7] "Galactic Discovery Project." *Galactic Discovery Project*. University of Washington.

[8] Dias, W. S., H. Monteiro, T. C. Caetano, and A. F. Oliveira. "Fitting Isochrones to Open Cluster Photometric Data." *Astronomy & Astrophysics* 539 (2012): A125. *NASA ADS*.

[9] Collins, George W., II. "Chapter 5." *Stellar Interiors*. N.p.: n.p., 2003. 112-48. Web. <http://ads.harvard.edu/books/1989fsa..book/AbookC05.pdf>.

[10] "Stars - Stellar Evolution." *Stars - Stellar Evolution*. Astronomy Online,

[11] "Nature of the Universe." *Nature of the Universe*. Hong Kong University,

[12] Glatzmaier, Gary A. *Introduction to Modeling Convection in Planets and Stars: Magnetic Field, Density Stratification, Rotation*. Princeton: Princton U, n.d. *Gary's Book*. University of Arizona.

[13] Spruit, H. C. "Essential Magnetohydrodynamics for Astrophysics." (2013): n. pag. *Henk's Preliminary Index*. Max Planck Institute for Astrophysics. Web. <http://www.mpa-garching.mpg.de/~henk/mhd12.zip>.

[14] The Sun." *The Sun*. University of Arizona. <http://ircamera.as.arizona.edu/astr_250/Lectures/Lecture_12.htm>.

[15] Howell, Steve B. *Handbook of CCD Astronomy*. Cambridge: Cambridge UP, 2006.

[16] Warner, Brian. *A Practical Guide to Lightcurve Photometry and Analysis*. New York: Springer, 2006.

[17] Notsu, Yuta. "Superflares on Solar-type Stars Observed with Kepler II. Photometric Variability of Superflare-generating Stars: A Signature of Stellar Rotation and Starspots - INSPIRE-HEP." *Superflares on Solar-type Stars Observed with Kepler II. Photometric Variability of Superflare-generating Stars: A Signature of Stellar Rotation and Starspots - INSPIRE-HEP*. Inspire

[18] Koch, David G., William J. Borucki, Gibor Basri, Natalie M. Batalha, Timothy M. Brown, Douglas Caldwell, Jørgen Christensen-Dalsgaard, William D. Cochran, Edna Devore, Edward W. Dunham, Thomas N. Gautier, John C. Geary, Ronald L. Gilliland, Alan Gould, Jon Jenkins, Yoji Kondo, David W. Latham, Jack J. Lissauer, Geoffrey Marcy, David Monet, Dimitar Sasselov, Alan Boss, Donald Brownlee, John Caldwell, Andrea K. Dupree, Steve B. Howell, Hans Kjeldsen, Søren Meibom, David Morrison, Tobias Owen, Harold Reitsema, Jill Tarter, Stephen T. Bryson, Jessie L. Dotson, Paul Gazis, Michael R. Haas, Jeffrey Kolodziejczak, Jason F. Rowe, Jeffrey E. Van Cleve, Christopher Allen, Hema Chandrasekaran, Bruce D. Clarke, Jie Li, Elisa V. Quintana, Peter Tenenbaum, Joseph D. Twicken, and Hayley Wu. "Design, Realized Photometric Performance, And Early Science." *The Astrophysical Journal* 713.2 (2010): L79-86.

[19] Meibom, Søren, Sydney A. Barnes, David W. Latham, Natalie Batalha, William J. Borucki, David G. Koch, Gibor Basri, Lucianne M. Walkowicz, Kenneth A. Janes, Jon Jenkins, Jeffrey Van Cleve, Michael R. Haas, Stephen T. Bryson, Andrea K. Dupree, Gabor Furesz, Andrew H. Szentgyorgyi, Lars A. Buchhave, Bruce D. Clarke, Joseph D. Twicken, and Elisa V. Quintana. "The Kepler Cluster Study: Stellar Rotation In Ngc 6811." *The Astrophysical Journal* 733.1 (2011): L9.

[20] "Custom Scientific Photometric Filters." *Custom Scientific Photometric Filters*. SBIG

[21] J. E. Van Cleve & D. A. Caldwell, Kepler Instrument Handbook (KSCI-19033).

[22] J. L. Christiansen, J. M. Jenkins, D. A. Caldwell, T. Barclay, S. T. Bryson, C. J. Burke, J. Campbell, J. Catanzarite, B. D. Clarke, J. L. Coughlin, F. Girouard, M. R. Haas, K. Ibrahim, T. C. Klaus, J. J. Kolodziejczak, J. Li, S. D. McCauliff, R. L. Morris, F. Mullally, E. V. Quintana, J. Rowe, A. Sabale, S. Seader, J. C. Smith, M. D. Still, P. G. Tenenbaum, S. E. Thompson, J. D. Twicken, and A. K. Uddin, 2013 , Kepler Data Characteristics Handbook (KSCI - 19040 - 004)

[23] Revision 5: D. Fraquelli & S. E. Thompson, 2014, Kepler Archive Manual (KDMC-10008-005).

[24] "Variable Star Plotter (VSP)." *AAVSO*. AAVSO,

[25] Scargle, J. D. "Studies in Astronomical Time Series Analysis. II - Statistical Aspects of Spectral Analysis of Unevenly Spaced Data." *The Astrophysical Journal* 263 (1982): 835